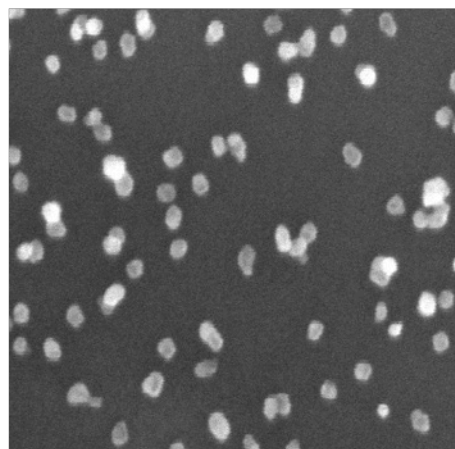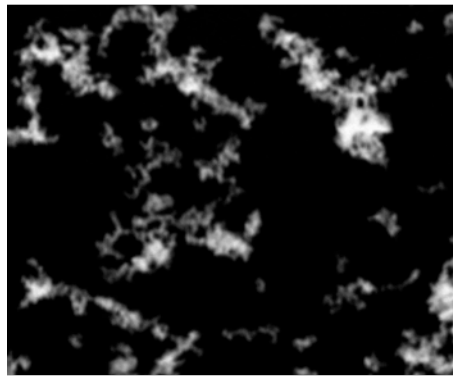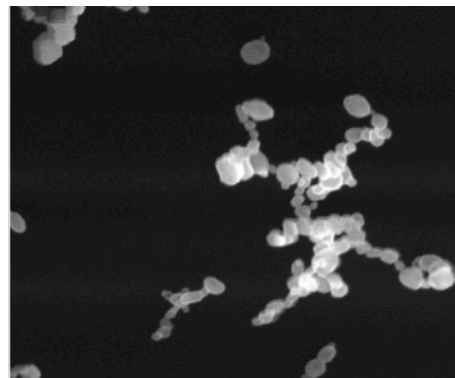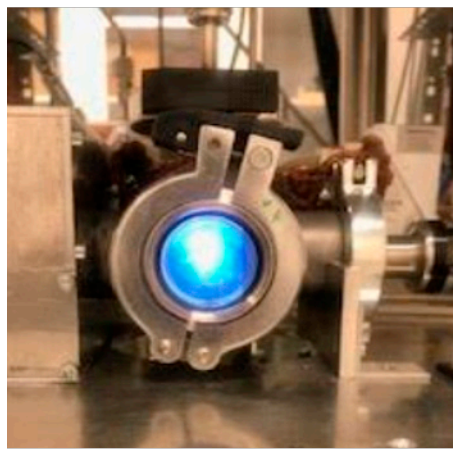# Generation of Model NiMo Hydrotreating Nano-catalysts via the Spark Discharge Technique

Hatoon Makhool

Department of Chemical Engineering
Master Thesis 2020

LUND UNIVERSITY

Generation of Model NiMo Hydrotreating Nano-catalysts via the Spark Discharge Technique

Master Thesis by Hatoon Makhool

Faculty of Engineering
Department of Chemical Engineering

June 2020

LUND
UNIVERSITY

Hatoon Makhool

# Generering av modell NiMo hydrering nano-katalysatorer genom 'Spark Discharge' Tekniken

Katalysatorer är viktiga komponenter i den kemiska industrin. Deras användning tillåter kemiska processer att ske på ett ekonomiskt och miljövänligt sätt, förutsatt att de är stabila och har bra aktivitet i den kemiska miljön där de tillämpas. Ett viktigt steg vid implementeringen av nya kemiska processer är alltså att utveckla lämpliga katalysatorer. Processen att utveckla sådana kan vara väldigt resurskrävande på grund av att det ofta finns många alternativa av katalysatortyper som ska utforskas, samt många variabler som dessa olika katalysatortyper ska undersökas för. Dessutom är tillverkningen av katalysatorer för endast testning miljöovänligt på grund av att kemikalieanvändning och höga katalysförädlings temperaturer vanligtvis är involverade.

För att undersöka möjligheten att optimera katalysatorutvecklingsprocessen genomfördes detta arbete med syftet att utforska potentialen av en resurseffektiv och miljövänligare metod att generera katalysatorer med egenskaper som liknar dem av de industriellt tillverkade katalysatorerna. Metoden som utforskades kallas för *'Spark discharge'* tekniken och den sker i enheter som kallas för *'Spark discharge Generators (SDG)'*. Genom den kan partiklar i nano-skala tillverkas relativt snabbt och utan behov för externa kemikalier. Principen bakom den tekniken är att orsaka förångning av material från elektroder som kopplas tvärs en elektrisk krets. Detta sker vid en tillräckligt hög spänning som resulterar i att området mellan elektroderna når en väldigt hög temperatur, vilket orsakar förångningen av elektrodernas material.

För att undersöka detta, har gynnsamma katalysatoregenskaper specificerats genom att granska en industriell fallstudie med bra katalysatorer. Den fallstudien var från en kemisk process som kallas för *hydrering*, i vilken kemiska reaktioner sker för att eliminera oönskade komponenter från råmaterial, såsom biomassa. De komponenterna, såsom svavel innehållande molekyler, är oönskade för att de kan orsaka skador på industriella enheter där biomassan vidare förädlas för utvinning av energi och kemikalier, samt i förlängning kan bidra till försurning av sjöar och vattendrag. De specificerade katalysatoregenskaperna från den fallstudien inkluderade, bland annat, sfäriska icke-agglomererade partiklar.

Försök har därefter genomförts för att undersöka om partiklar med de specificerade egenskaperna kunde genereras från SDG-systemet. En ugn kopplades till systemet för att vidare förädla de genererade partiklarna. Partiklarna utvanns slutligen på en yta mot vilken de transporterades med hjälp av en bärgas, vilket möjliggjorde deras karakterisering med mikroskopiska och spektroskopiska metoder.
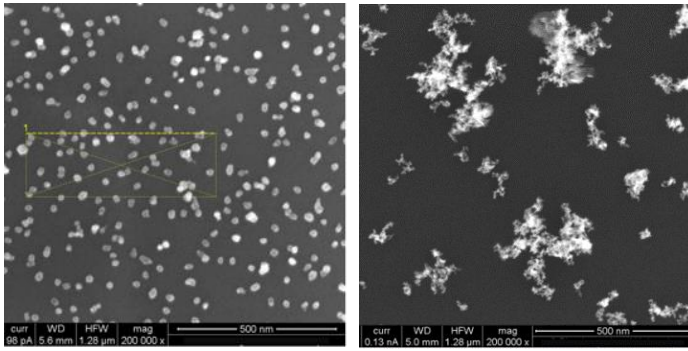
Figur 1 visar exempel på genererade nano-partiklar med olika egenskaper.

Olika systemparametrar, såsom elektrodstyper med olika material och ugntemperaturer, testades vid försöken. Mikroskopiska och spektroskopiska analyser på de utvunna nano-partiklarna visade att olika system driftsparameter gynnar partiklar med olika egenskaper. I figur 1 visar figuren till vänster ett prov med sfäriska NiMo nano-partiklar, vilka lämpar sig för användning som modell nano-katalysatorer. Provet erhölls genom att använda en Ni_3Mo_7 elektrod med en Mo elektrod, 2.5 kV elektrisk spänning och 1200 °C ungtemperatur. Figuren till höger visar ett prov med agglomererade strukturer som inte är gynnsamma och detta erhölls genom att istället använda två Ni_3Mo_7 elektroder, 1.4 kV elektrisk spänning och 1000 °C ungtemperatur. Slutligen identifierades den systemparameterkombinationen som gav nano-partiklar med de önskade egenskaperna och som i framtida experiment kan tillämpas för att generera partiklar med liknande egenskaper för möjligtvis katalytiska tillämpningar.

Abstract

_____

Establishing a technically practical method to generate representative model catalysts for the use in characterizations and testing prior to catalyst implementation in chemical process units would allow for a more sophisticated understanding of the underlying catalytic mechanisms. As a step towards establishing such a method, generating non-agglomerated, spherical NiMo nanoparticles, with diameters below 25 nm and atomic composition of maximum 30 at% Ni with Mo (maximum 3:7 Ni:Mo atomic ratio), for application as model hydrotreating catalysts, was addressed. The investigated method for the generation of these model nano-catalysts was the Spark discharge technique. The generation of nanoparticles through this method is carried out by employing an electric circuit, across which electrodes are connected and evaporate upon the application of a sufficiently high voltage. A furnace and a deposition chamber were also incorporated post the Spark discharge chamber to improve the morphological properties of the generated nanoparticles via sintering, and to yield supported nanoparticles for further characterizations of the nano-catalysts through SEM, EDXS and XAS.

Combinations of different system parameters were tested to deduce how the morphological and compositional characteristics of the nanoparticles are affected by these, including parameters in the electric circuit and furnace temperature.

Nanoparticles with variable characteristics were followingly yielded upon employing the different parameter combinations. Among these, non-agglomerated, spherical nano-catalysts with an average diameter of about 19.6 nm were generated as desired. The obtained compositions were 3:7 and 1:4 Ni:Mo atomic ratio. Finally, the parameter combination that produced nanoparticles with the desired properties was determined and discussed in detail. Additionally, as a means of assessing the suitability of the generated nanoparticles as nano-catalyst, the reducibility of the Ni and Mo in the nano-catalysts was examined and compared to that of industrial references.

Acknowledgements

_____

Table of Content
_____

List of Figures

_____

List of Tables

_____

Chapter 1: Introduction
_____

1.1 Insight into Catalyst Development

Effective catalysis is an essential element in the chemical and petrochemical industry as the process of catalyst development and implementation highly contributes to the overall costs of commercial industrial processes. As an example, biomass conversion is one area that is still under development, partially due to the need for finding suitable industrial catalysts for application in the biomass conversion and treatment units. The process of finding suitable catalysts is a costly long-term one. Besides, following the usual catalyst development processes can be very inefficient, as many of the detriment functional parameters of a catalyst cannot be considered at an early development stage. Such parameters include catalyst selectivity, longevity and deactivation mechanisms. Establishing an efficient catalyst development method that follows methodological approach and that considers different catalyst parameters, already at an early development phase, will transform the catalysts development process into a more efficient one [1]. Consequently, this will, for example, facilitate a faster and more techno-economic development process for biomass conversion, enhancing the progress in the process of fully converting to a greener chemical and fuel industry in the near future.

Currently, catalyst development follows an experience-based trial-and-error approach, where catalyst screening for activity is the primary focus. Other complexities such as catalyst activation, selectivity, poisoning and fouling are not. The detection of any of the latter named complexities post-catalyst adoption can give rise to unexpected process complications and costs, proving the adopted catalyst to be unsuitable for achieving the industrially desired economic profit. Such scenarios also mean that higher cost uncertainties will be associated with new chemical processes under development.

Moving beyond this trial-and-error approach by combining experience, computational, chemical and analytical methods to establish a more techno-economical and structured catalyst development method will lead to a better understanding of the different actors of the optimization problem at an early phase of the development process. Thus, unexpected latter costs and technical problems will be avoided. [1]

1.2 Thesis Background

This work was part of a research project with the goal of establishing a method to develop model catalyst systems. Nanoparticles had thus been researched as potential model catalysts. The research background and nanoparticles as catalysts are considered in 1.2.1-1.2.2.

1.2.1 Research Background

Developing a method for the development of industrial catalysts has been the research area of a group of researchers, led by Sara Blomberg and Christian Hulteberg, at Lund University. As part of this, generating model catalytic nanoparticles with specific characteristics, similar to those of

bulk catalysts, via the spark discharge technique is being studied. When fully understood and established, the generation of well-defined model nano-catalysts for use during catalyst development tests will be simpler and purer. Besides, having a well-defined catalyst model system will facilitate further experimental catalyst characterizations for clearly defining the underlying catalysis mechanisms.

The type of catalysts that are being studied are hydrotreating nickel-molybdenum (NiMo) catalysts. To identify the exact desired characteristics that the model catalyt nanoparticles must exhibit, data on industrial NiMo catalysts were obtained from an industrial biomass hydrotreating case study. The obtained industrial data was applied in in-silico simulations where different catalyst properties were examined to finally specify the chemical and physical characteristics which make these good catalysts and which the model nano-catalysts being generated must exhibit to show as good catalytic functionality as the industrial ones. The physical and chemical properties were specified as NiMo nanoparticles as small as possible in size, below 30 nm in diameter, with atomic composition of maximum 3:7 Ni:Mo (i.e. maximum 30 at% Ni with Mo). Also, sphericity and as little agglomeration as possible are required to maintain an efficient catalytic surface area.

As the following step to these simulations, attempts to generate NiMo model nano-catalysts with the mentioned characteristics, via the spark discharge technique, were performed. Particles with sizes of 25 nm in diameter and approximate atomic Ni:Mo compositions of 7:3 were yielded [2]. However, as the initial *in-silico* simulations indicated, smaller particles with higher Mo compositions would show a better catalytic performance, it was concluded that further experimental work to produce model catalysts with better characteristics was required. To do this, the effect of the different parameters of the synthesis system on the characteristics of the generated nanoparticles must be understood in order to determine the parameters that produce particles with the desired characteristics for application as model hydrotreating nano-catalysts.

1.2.2 Nanoparticles as Catalysts

Recently, research within nanoparticle generation techniques and applications have been evolving. Nanoparticles have been generated via both sol-gel techniques and gas-based ones. Adopting different techniques was found to affect the quality of the product, where the latter named technique usually yields purer particles as liquid components, otherwise involved in sol-gel techniques, are not used. Nanoparticles have different application areas, one of which is catalysis [3]. This includes thermochemical catalysis processes such as reduction, electrochemical and photocatalysis [4]. The catalytic potential of nanoparticles could be attributed to the special physical characteristics that they exhibit compared to particles of higher dimensions. These special characteristics include larger surface-area-to-volume ratios, lower melting points and higher self-diffusion coefficients [3], [5].

However, a major challenge is to find ways to generate catalytic nanoparticles without agglomeration to ensure efficient catalysis. It was reported that nanoparticles have a high tendency

to agglomerate during generation, decreasing their effective surface area. Controlling the size and morphology of the nanoparticle during generation is thus necessary to avoid inefficient surface area-to-volume ratios. [4], [6]

1.3 The Aim of the Thesis

As a step towards obtaining NiMo nano-catalysts with morphological and compositional specifications that are similar to those of the industrial case study, this work was carried out with the aim to:

- o investigate how the morphology (size and shape) and composition of the spark discharge generated NiMo nanoparticles are affected by different synthesis system parameters and combinations thereof,
- o determine which parameters (levels) give particles with sizes (diameters) of 25 nm or below and a maximum atomic composition of 30 at% Ni with Mo,
- o employ the established parameters to generate model catalysts for further catalyst characterizations.

Working towards the aim of this project, a theoretical review on the hydrotreating process, its catalysts and the Spark discharge technique was carried out. This is described in Chapter 2.

Chapter 2: Theory

2.1 NiMo as a Hydrotreating Catalyst

Hydrotreating is the removal of sulfur (hydrodesulfurization), nitrogen (hydrodenitrogenation), oxygen (hydrodeoxygenatiom), among other undesired components, from coal, oil or biomass feedstocks. This occurs via hydrogenation, hydrogenolysis and/or elimination reactions under suitable H_2 pressure, temperature, catalysts such as NiMo, etc [7]. The primary purpose of this feedstock treatment step is the elimination of system poisoning components. Several different reactions can take place in a hydrotreating unit. Examples of these reactions are presented in Appendix I. The extent to which each reaction type is required is determined by the quality of the feedstock that is being hydrotreated. For example, biomass is relatively rich in oxygen-containing compounds [7], dictating that sufficient hydrodeoxygenation must occur to obtain a high-quality feedstock. The different types of reactions can possibly be enhanced by means of controlling the system parameters and hydrotreating unit design [8].

Hydrotreating occurs at high temperatures and pressures [9], [8]. As it is an essential step for upgrading feedstocks, improving the process conditions, for example by improving the employed catalysts, will contribute to the optimization of the overall biomass conversion process.

NiMo is one catalyst that was found to be suitable for biomass hydrotreating, yielding upgraded biomass feedstock with less sourness and corrosivity, as well as less chemical complexity [9]. In one study that investigated the catalytic activity of NiMo, different NiMo/ γ-Al_2O_3 catalyst compositions were compared in order to determine the most active one. The varied compositions were Ni:Al_2O_3 and Ni:Mo as reported, and in one of the studied cases, no Mo was used in the catalyst. The results revealed that adding Mo improved the Ni catalytic activity, demonstrating the activity of NiMo catalysts in biomass hydrotreating. [9]

Even though NiMo catalytic activity was proven, the exact catalysis mechanisms, including the promoting components and active sites, are still not fully understood. It was however suggested that the nature of the catalytic mechanisms is determined by the catalyst activation step known as sulfidation [10]. In sulfidation, a feed containing hydrogen and a sulfur-containing compound is employed to obtain a sulfidic metal phase, which acts as the catalytically active phase [8].

One active sulfidic catalyst structure that was suggested to form during sulfidation, and later on determine the active site mechanism, is a nickel-molybdenum-sulphide phase, expressed as Ni-Mo-S, as revealed by Density-functional Theory (DFT) calculations [7]. In this structure, the Ni ions are located at the edges of MoS_n crystallites. In some research, the activity of this phase was attributed to the loss of edge, Mo-attached S ions, giving S-vacancies. These vacancies then act as active sites. In other studies, it was furthermore suggested that the S-vacancies occur due to the net bond strength of S bonded to one Mo and one Ni being less than that of S bonded to two Mo

ions. That is; S-vacancies can more easily form when Ni is added to Mo, implying that Ni is the promoter. [7]

Whenever intending to understand such structures and mechanisms, complications usually arise due to the complexity of the catalyst structure, making it difficult to identify through common solid phase characterization techniques. Also, catalysts are highly affected by the nature of their treatment and activation steps, as explained above, where their structures, among other properties, are manipulated. This makes it difficult to generalise findings in terms of catalyst properties post-treatment from one case to the other. Thus, understanding and establishing a simple method to generate model catalysts, with properties that are similar to those of the industrial ones, means that model catalysts for testing can easily be generated in the future to represent different industrial cases. This will eliminate the need for making inaccurate assumptions and generalisations.

2.2 Spark Discharge Generation

The generation of nanoparticles through the spark discharge technique occurs in Spark Discharge Generators (SDGs). The technique is generally simple and is suitable for generating pure nanoparticles [11]. It is also highly environmentally friendly [2], as no chemicals are needed, and no emissions are released during operation.

The SDG setup mainly involves electrodes connected across an electric circuit that is normally consisting of resistance (electrode gap and external resistor if required), capacitance and inductance (RCL circuit) [11]. The SDG setup is depicted in Figure 1.
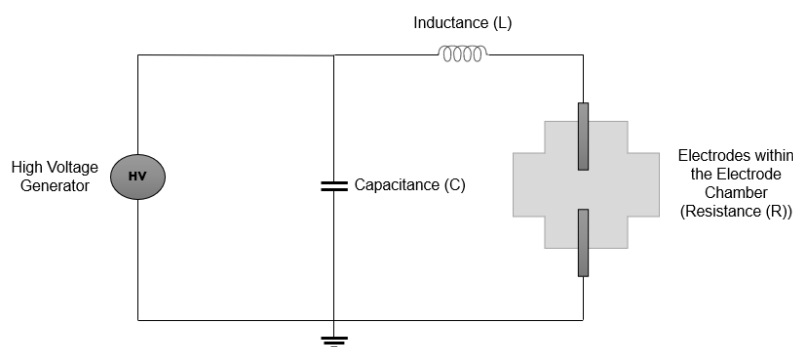
Figure 1. The RCL circuit and the electrodes chamber.

In SDGs, the source of the generated nanoparticles is the material of the electrodes that are connected across the electric circuit. The nanoparticle generation mechanism starts by firstly applying a specific voltage above a breakdown voltage. This is provided by setting suitable circuit parameters (voltage, current and resistance). When a high enough electric field is present across the electrodes, electrons are ejected, together with charged ions, at a sufficiently high acceleration, leading to the ionization of multiple gas molecules between the electrodes. When the ionization level is high enough, a high concentration of charged particles between the electrodes forms and

results in a conducting plasma channel, conducting current between the electrodes. Finally, a spark forms due to the inter-electrode current flow through the plasma channel. The formed spark can last for some time (microseconds) depending on the circuit parameters and it can reach local temperatures as high as 20,000 – 30,000 K. At these high temperatures, the material of the metallic electrodes evaporates, generating nanoparticles within the inter-electrode volume.

It is important to note that the term evaporation is used in this context as it was used in other similar contexts in the reviewed studies. However, evaporation generally applies to a change in state from liquid to gas, which is not likely the case for the particle generation mechanism in the SDG-system. For simplicity, the term evaporation will be used in this report to indicate the generation of particles from the electrodes, but not to indicate a liquid-to-gas state change.

During the spark period, the inter-electrode volume becomes more and more concentrated with particles. As this happens, collisions between the particles occur, leading to coalescence. The particle concentration determines the level of supersaturation at the inter-electrode volume and different levels of supersaturation lead to different levels of coalescence. These are referred to as complete and partial coalescence. Low supersaturation levels favor complete particle coalescence, which results mostly in spherical particles (primary particles). A high level of complete coalescence leads to an increase in the sizes of the primary particles. Partial coalescence, on the other hand, is more likely to occur when a high supersaturation level is achieved, and it results in the agglomeration of primary particles (necking). [11]

To mobilize the generated particles away from the inter-electrode region, a carrier gas is used. The particles are then carried along with the gas towards downstream units, such as a furnace often used for the purpose of sintering. The particles may even be deposited on a substrate, making further morphological and compositional analysis possible.

There are several system operation parameters that can significantly affect the final characteristics of the generated particles, including the parameters of the electric circuit and the type of electrodes. However, incorporating other processing units downstream give rise to other influencing parameters. For example, if a furnace is employed, it can be operated at different temperatures, which affects how the particles are sintered. Other parameters, such as the carrier gas type and flow rate, can also influence the final properties of the particles.

In this work, the SDG system was connected to a furnace, an electrically on-substrate particle collecting chamber and particle counters. The exact employed system is considered in details in later chapters, but in order to understand the effect of the different operation parameters, a literature review describing the effect of the electrode types, electric circuit, carrier gas and furnace parameters on the generated nanoparticles is presented in the following sub-sections.

2.2.1 Effect of the Electrodes

The physical and chemical properties of the electrode, including the electrode chemical composition, the metal ionization potential, electrode polarity and the evaporation enthalpy, were found to have a detrimental effect on the generated particles.

The composition of the electrodes certainly influences that of the yielded nanoparticles. This was confirmed in several studies where mono- and bi-metallic electrodes were used [2, 3, 12]. As an example, NiMo nanoparticles were generated using one nickel and one molybdenum electrode in combination [2], confirming that the components in the produced particles are similar to those of the employed electrodes. These particles also showed a larger Ni atomic ratio [2], indicating that the rate of Ni electrode evaporation was higher, probably due to Ni having a lower boiling point and evaporation enthalpy than Mo. See Appendix I for a list of the physiochemical data of Ni and Mo.

In one investigation, the effect of the evaporation enthalpy of the metals on the particle size distributions was studied for different metals under otherwise similar system operation parameters. It was reported that metals like antimony and magnesium showed high spark erosion in comparison to other metals like tungsten. This was related to the molar evaporation enthalpy of the metals, which is much lower for antimony and magnesium in comparison to that of tungsten, concluding that the lower the evaporation enthalpy is, the higher the rate of loss of electrode material is. [3]

The ionization energy of the materials of the electrodes was also found to influence the particles when different mono- and bi-metallic nanoparticles of gold, silver, platinum and palladium were generated. For the monometallic nanoparticles (in particles/cm^3), larger particles, with a higher particle concentration, were obtained for metals with higher ionization potentials. For bimetallic particles, the obtained size distributions fell between those of the individual monometallic particles. An interesting observation based on the presented bimetallic particles data was that placing the metal with the higher ionization potential on the anode side resulted in larger particles. Furthermore, the composition of the final nanoparticles was composed of more of the anode material than the cathode material. [12]

In another reviewed study, a higher weight percentage of the material of the cathode (negative electrode) was found in finally yielded gold-platinum particles, opposing the findings of the previously described study. [13] Thus, this remains uncertain and further investigation is required.

2.2.2 Effect of the Circuit: Resistance, Capacitance, current and voltage

The main parameters of the electric circuit in SDGs are the resistance (corresponding to the gap between the electrodes), the capacitance, the current and the voltage, as mentioned earlier. The resistance, capacitance and voltage are directly related to the spark energy and frequency, which in turn indicate the electrode material loss, supersaturation and/or coagulation levels in the inter-

electrode region, determining the finally yielded particle concentrations and size distributions [11, 14].

The higher the spark energy is, the higher the energy available for the material of the electrodes to evaporate is [11]. Also, the higher the spark frequency is, the smaller the generated particles are [14]. To examine these statements, the relations between the spark energy and frequency with the circuit parameters were studied by considering developed mathematical equations. Equation 1-2 describe how the spark energy varies with the capacitance and the voltage across the circuit and equation 3 describes how the frequency varies with the current and capacitance [11].

$$E = \frac{1}{2} * C * V_d{}^2 \qquad (1)$$

where,

$$V_d = V_b + V_o \qquad (2)$$

E is the spark energy, C the capacitance and V_d the discharge voltage. V_d is the sum of the breakdown voltage V_b and an overvoltage V_o. V_b is the minimum voltage required for a spark discharge to occur. V_o is due to energy losses.

$$f = \frac{I}{C * V_d} \qquad (3)$$

f is the spark frequency, I the current, C the capacitance and V_d the discharge voltage.

As described by equation 1 and 3, the spark energy is directly proportional to and increases with the capacitance and the discharge voltage squared, while the spark frequency increases with increasing the current and decreasing the capacitance and/or the discharge voltage.

The resistance is often considered as the inter-electrode gap. The inter-electrode gap size was related to the breakdown voltage through Paschen's law [11]. In this law, the breakdown voltage varies with, beside the gap size, the gas type and pressure as described by equation 4 [11].

$$V_b = \frac{B * p * d}{\ln \frac{A * p * d}{\ln(1 + \frac{1}{\gamma})}} \qquad (4)$$

V_b is the breakdown voltage, d the inter-electrode gap and p the gas pressure. A, B and γ are gas-dependent parameters.

Equation 4 reveals that increasing the gap distance will increase the breakdown voltage, which will also increase the spark energy based on equation 1.

The effect of varying the inter-electrode gap size was determined during the generation of gold nanoparticles. It was concluded that the spark energy and the electrode material loss increased with increasing the inter-electrode gap size (resistance), agreeing with the trends revealed by equation 1

and 4. Parallel to these observations, a particle distribution with a larger mean particle diameter was obtained as the gap was increased. [3]

The spark frequency was related to the evaporation of the electrode material. No significant effect on the mean particle sizes was detected due to changing the spark frequency, but varied distribution curve broadness and peak heights were detected. At the same particle mean size, the number of particles with the mean size increased until the spark frequency value of 30 Hz, after which a lower number of mean sized particles was obtained at a frequency of 80 Hz. [3]

2.2.3 Effect of the Carrier Gas

The carrier gas is used for flushing out the formed nanoparticles away from the SDG chamber to following downstream units. It was demonstrated in several experimental scenarios that the gas type, as well as the flow parameters, affect both the properties of the generated nanoparticle and their purity.

Oxides are the major contaminants of metallic nanoparticles. Usually, inert gases like Argon and nitrogen are used to avoid gas-particle reactions. However, gaseous mixtures including hydrogen, such as nitrogen with some hydrogen, are often used instead of pure inert gases to limit the oxidation of the nanoparticles. Pure argon was used as the carrier gas during the generation of copper and tungsten nanoparticles and impurities of metal oxides (W_xO and CuO_x) were detected [13], suggesting a higher likelihood of oxygen-based phase contaminations in the absence of hydrogen.

Regarding the effect of the gas on the particle size, Paschen's law (equation 4) represents one mathematical formulation on how the gas type and gas pressure affect the breakdown voltage, which in turn affects the spark energy (equation 1-2). The effect of the gas type was previously investigated for a specific gap size and different gases. The breakdown voltage was found to decrease in the order nitrogen, air, argon and helium [3]. Considering this together with the spark energy and discharge voltage relations shown in equation 1-2, the spark energy must increase when using a gas type like nitrogen, which has a high breakdown voltage. Followingly, more evaporation of the electrode material and larger particles can occur.

The effect of the gas pressure, as described in equation 4, is to increase the breakdown voltage as it is increased. However, most of the reviewed studies regarding this aspect report the effect of the gas flowrate rather than the gas pressure.

In one such experiment where the effect of the flowrate was examined, the particle (modal) diameter decreased in an exponential manner with increasing the volumetric gas flowrate. At about 5 L/min, the obtained particle diameter was about 4 nm. This was attributed to that a high gas flowrate probably enhances the cooling and dilution rates (decreasing supersaturation) between the

electrodes, enhancing the generation of smaller nanoparticles. Besides, narrower particle distributions were obtained at high flowrates, which was attributed to less coagulation occurring in the diluted regions. [3]

The particle size in terms of geometric mean diameter was also suggested to change with the gas properties and flowrate in accordance to the principles of conversion of mass per unit volume in combination with Feng's model; an analytical model that suggests that the particle concentration decreases with increasing the coagulation time. This is directly related to the gas flowrate as increasing the flowrate decreases the residence time of the nanoparticles in the inter-electrode region. Consequently, the time available for the particles to interact and undergo coagulation decreases, resulting in smaller non-agglomerated particles. The mathematical relationship for the particle geometric mean diameter is presented in equation 5. [14]

$$\overline{D_p} = 3.75 * 10^{-6} \left(\frac{\dot{m}*V}{\rho*\dot{v}}\right)^{0.267} \tag{5}$$

D_p is the geometrical particle size (2-20 nm), $\dot{m}$ the mass loss rate from the electrode, V the volume where coagulation can occur and it is referred to as the coagulation volume (mainly SDG chamber), ρ the gas density and $\dot{v}$ the volumetric flowrate of the gas.

Equation 5 demonstrates that decreasing the expression inside the brackets: increasing the gas density and/or the gas volumetric flowrate decreases the particles mean size. [3]

2.2.4 Effect of the System dimensions

The main system dimensions include the electrodes dimensions, inter-electrode gap and the coagulation volume which is mainly in the SDG chamber.

The electrode dimensions are of great importance based on practical experience and observations of several SDG-researchers. As described above, the plasma formation leads to a spark generation which heats up and evaporates the electrode material. The volume of the electrodes that is being effectively heated by the spark, the hotspot, depends on the dimensions of the electrodes, including the diameter and length. Consequently, the electrode thickness and length influence the level of evaporation from the electrode material.

Llewellyn Jones 1950 [15] suggested a model which explains the link between the dimensions of the electrodes and their potential to evaporate. Based on this model, energy input into a solid material is dissipated via the conduction of heat to the surrounding, radiation and/or evaporation. The level of conduction is enhanced by the material volume and thus lower net conduction occurs when smaller electrode volumes are used. This means that more of the energy that is transferred to the electrodes can be dissipated via evaporation, as well as radiation, if electrodes with small volumes are employed.

10

The dimensions of the SDG chamber are also important as these determine the volume available for particle coalescence and agglomeration to take place. These dimensions also affect the purity of the products as small volumes mean that the spark heat will more likely reach and effectively heat the walls of the system, leading to the loss of material from the walls. This material can followingly contaminate the product. Analytically, the effect of the system dimensions on the particle sizes was also considered in equation 5 such that decreasing the volume available for agglomeration can decrease the particle geometrical mean diameter [14].

However, manipulating the dimensions of the SDG system is not possible in the studied system, which will be described in Chapter 3.

2.2.5 Effect of the Downstream Furnace

As mentioned above, a furnace can be mounted downstream after the SDG chamber to modify the characteristics of the particles via sintering. In the furnace, the employed temperature and likely the dimensions, can affect the final particle characteristics. However, most of the reviewed studies focus on the effect of the furnace temperature rather than the furnace dimensions and accordingly, the effect of the temperature is the main focus of this sub-section.

In one experimental work, increasing the sintering temperature that was employed in a tube furnace of 0.03 m diameter and 0.5 m length decreased the particle sizes and aggregation, as well as improved the sphericity of the particles. The largest size reductions were 155 to 80 and 70 to 17 nm, which were observed upon increasing the temperature from 100 to 250, respective 900 to 1000, revealing that the higher the furnace temperature is, the smaller and more spherical the generated particles become. [6]

Similar effects were reported in other studies, as it was concluded that using a heated tube after the SDG chamber generates spherical particles with reduced agglomeration levels [14].

Besides the morphological properties, the sintering temperature can possibly affect the composition and atomic structure of the particles. Generally, bulk solid mixtures exhibit different phases with different structures at different temperatures. At the nanoscale, this is possible, especially that nanoparticles have reduced boiling and melting points, as well as higher diffusivities [3, 5], allowing them to possibly adopt special structural patterns and compositions at higher temperatures.

To investigate these relations, experiments were designed to study the effect of chosen system parameters on the characteristics of NiMo nanoparticles. These are described in detail in Chapter 3 and 4.

Chapter 3: Experimental Methodology

3.1 Experimental System

The employed experimental system was built up by the Researcher Engineer Bengt Meuller at Lund Nano Lab facility and is presented schematically in Figure 2.
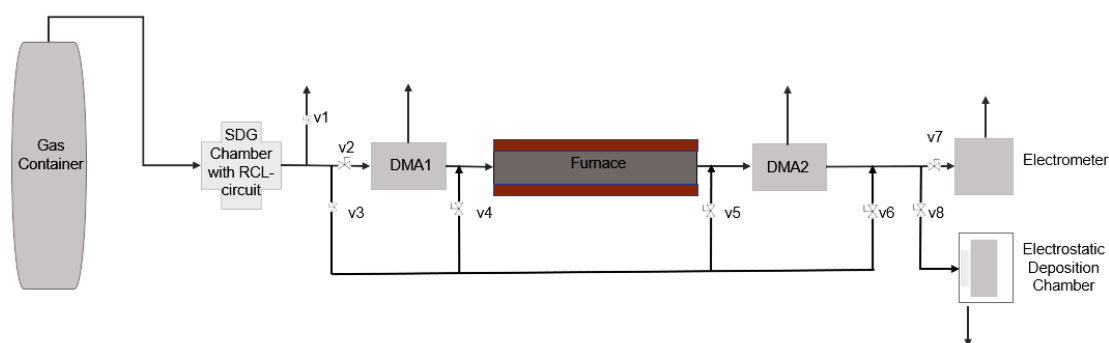
Figure 2. Schematic diagram of the experimental system for the generation of the NiMo catalytic nanoparticles.

The heart of the system that is presented in Figure 2 is the SDG chamber, where the nanoparticles form. The SDG chamber houses the metal electrodes, which are connected across the RCL-circuit. The generated nanoparticles are purged out of the SDG chamber by employing an inert carrier gas, supplied from the gas container. A furnace is connected downstream for the purpose of sintering the nanoparticles. Two Differential Mobility Analyzers (DMA) are connected before respective after the furnace, serving as particle selectors after particle size. The particle selection occurs via creating electrostatic forces between the walls of the DMAs which are charged, and the nanoparticles which have different sizes and charges. Particles with the desired sizes are carried along with the carrier gas to the following system units, while the undesired particles are excluded from the system.

After DMA2, an electrometer and an electrostatic deposition chamber are connected in a parallel configuration. The electrometer serves the purpose of counting the number of particles by detecting the net number of negative charges. The electrostatic deposition chamber is made of a flat metal surface, where a substrate/wafer is placed, towards which nanoparticles are electrostatically attracted and deposited.

As demonstrated in Figure 2, by-passing DMA1, DMA2 and/or the furnace is possible by opening or closing the manual valves that are mounted on the couplings (v2-v6). Similarly, the nanoparticles were either allowed to flow into the electrometer for getting a reading over the particle count or to the deposition chamber for deposition onto a substrate by controlling v7 and v8.

This system was automatically controlled by a sequence that is implemented into LabView, which was also developed by Bengt Meuller. Using this software, desired experimental parameters, including the flowrates through the different units and the discharge current, were specified. As an exception, the DMAs and the depositing voltage were specified locally through the devices instead of through the software due to detected software-to-system signal errors. However, all system-to-software signals were successful with no errors. Therefore, as output, readings of the discharge voltage, discharge current, pressure, the sizes of particles released by the DMAs, as well as the particle count of the generated particles could be obtained for system control and/or for use as results. The furnace temperature was also specified locally through a heater as this unit was not connected to the software. Likewise, the monitoring of the furnace temperature was done by registering the reading provided on the heater.

This system was employed as it produces relatively pure nanoparticles with very little environmental print, as it was mentioned earlier.

3.2 Experimental Methodology

The experimental work was planned such as to fulfill the research aim of finding the system parameters that would produce spherical NiMo nanoparticles with a maximum size of 25 nm in diameter and with a maximum atomic composition of 3:7 Ni:Mo. Other factors that were considered during the experimental planning include machine availability, experiments average duration, characterization methods restrictions and time requirements. Physical and practical system limitations, such as a maximum allowable furnace temperature of 1200 °C, using 1.68 L/min as the gas flowrate through the DMAs and particle counter, and a minimum allowable particle size of 10 nm through DMA2 were also accounted for.

Considering these factors, the independent variables were identified, and the experiments were planned as described in sub-sections 3.2.1-3.2.3.

3.2.1 Choice of Variables

The main dependent variables were the nanoparticles morphology (agglomeration, sphericity and size) and their composition. For investigating the morphology, six parameters were chosen as the independent variables. Whilst for the composition, one variable was chosen as the independent variable. Each of the independent parameters was tested at two levels.

The parameters that were chosen as independent variables for the morphology of the nanoparticles are the following.

- o   The material of the electrodes
- o   The discharge voltage
- o   The flowrate of the carrier gas through the SDG chamber
- o   The furnace temperature
- o   The depositing voltage
- o   The number of DMAs employed in the system

The parameter that was chosen as the independent variable for the composition was the material of the electrode.

The material of the electrodes was chosen for investigation as the literature review revealed the importance of the composition of the electrodes on that of the generated nanoparticles, as well as the influence of the physiochemical properties of the material on the amount of the generated nanoparticles (see Chapter 2). This variable was manipulated by simply mounting the desired electrodes at the beginning of each experiment. The studied electrode combinations were Ni_3Mo_7 with Ni_3Mo_7 and Ni_3Mo_7 with Mo. These are referred to as NiMo-NiMo and NiMo-Mo respectively in the rest of the report. Note that whenever NiMo-Mo electrodes were used, Mo was placed at the anode side.

The discharge voltage was studied as it was found to be correlated to the spark characteristics and thus influences the size of the forming nanoparticles (see Chapter 2). The discharge voltage was varied by adjusting the inter-electrode gap size. This gap effect was demonstrated in equation 4, where increasing the gap increased the discharge voltage. The employed system, however, lacked a regulation system for maintaining the inter-electrode gap unchanged. Thus, the gap gradually increased during operation, resulting in a gradual increase in the discharge voltage, which was detected by monitoring the variable readings. To maintain the desired discharge voltage value throughout the operation time constant, manual adjustment to decrease the inter-electrode gap was carried out whenever an increase in the discharge voltage reading was detected. The studied discharge voltage levels were around 1.4 and 2.5 kV.

Recall that the inter-electrode gap corresponds to the resistance in the electric circuit, and as this was controlled in order to maintain the desired discharge voltage, the resistance of the system was considered a constant variable.

The carrier gas flowrate through the SDG chamber was also found to be an important parameter based on the reviewed literature. Its variation was correlated to final sizes and shapes (agglomeration) of the nanoparticles (see Chapter 2). This variable was simply manipulated by setting the desired value in the LabView GUI. The studied flowrates through the SDG chamber were 1.68 and 4.00 L/min N_2. However, based on system limitations in terms of DMA calibrations, the flowrate through the DMAs was always supposed to be maintained at 1.68 L/min, which dictated that variations in the flowrate could only be done for the SDG chamber volume. Thereby, when 4 L/min was tested, splitting and excluding part of the gas prior to DMA1 was thus carried out to maintain the flowrate at 1.68 L/min through both DMAs, meanwhile employing the desired flowrate through the SDG chamber.

The furnace temperature was reported to have an effect on the sintering level of the nanoparticles and it thereby influences the sphericity and the level of agglomeration, of the generated nanoparticles. It possibly also affects the particle composition as explained in Chapter 2. Based on

this, the furnace temperature was chosen as a variable for investigation and it was varied by specifying the desired temperature on the heater. The investigated temperatures were 1000 and 1200 °C.

The depositing voltage was also seen detriment as it expectedly affected the distribution of the particles on the substrate. Even though not thoroughly considered in the reviewed literature, the depositing voltage was suspected of imposing influence on the deposition way of the nanoparticles. Since they were obtained and characterized as deposited on the substrate, it was thought that the force attracting the particles towards the surface must have had an influence on how the particles were positioned and perceived during the analysis. To investigate this, this variable was varied by locally adjusting the applied voltage acting on the deposition chamber. The investigated depositing voltages were 4 and 7 kV.

The number of DMAs in the system determines the final possible particle count and thus, the distributions of the sizes of the particles that were yielded on the substrate. To investigate the effect of employing different number of DMAs, experiments with one or both DMAs employed were carried. When one DMA was employed, DMA1 (Figure 2) was by-passed, otherwise both DMA1 and DMA2 were used.

Other system variables, including discharge current, pressure, carrier gas flowrate through the furnace, type of carrier gas, inter-electrode gap and substrate material were kept constant. A summary of the varied parameters, as well as the levels at which these were varied, and the unvaried parameters are presented in Table 1.

Table 1. A summary over the varied and constant parameters in the experiments.

	Parameter	Level(s)	Dependent variable
Independent variables	Material of the electrodes (E)	NiMo-NiMo and NiMo-Mo	-Shape and size -Composition
	Discharge voltage (V)	1.4 and 2.5 kV	Shape and size
	Flowrate of the carrier gas through the SDG chamber (F)	1.68 and 4.00 L N_2/min	Shape and size
	Furnace temperature (T)	1000 and 1200 °C	Shape and size
	Depositing Voltage (D)	4 and 7 kV	Shape and size
	Number of DMAs (n)	1 DMA (DMA2) and 2 DMAs (DMA1 and DMA2)	Shape and size

Constant Variables	Discharge current	8-15 μA	–
	Pressure	1.015 kPa	–
	Carrier gas flowrate through the DMAs, furnace and particle counter	1.68 L/min	–
	Type of carrier gas	N_2	–
	Substrate for the deposition of nanoparticles	SiOx	–

3.2.2 Experiment and Characterization Plan

The developed plan involved obtaining samples from experiments for Scanning Electron Microscopy (SEM) characterizations for particle shape and size, Energy Dispersive X-ray Spectroscopy (EDXS) for compositional analysis and X-ray Absorption Spectroscopy (XAS) for additional nano-catalyst characterization. The general planned steps were as listed below.

1. Carrying out experiments with different parameter combinations, such that for each independent variable, its two investigated levels are tested in two separate experiments, in which the rest of the parameters (all except the tested one) are employed at similar levels.
2. Characterizing samples that are obtained from experiments in (1) through SEM to deduce qualitative and quantitative morphological conclusions.
3. Carrying out more experiments to understand how the material of the electrodes affect the composition of the particles.
4. Characterizing samples from the experiments in (3), using EDXS, to deduce compositional conclusions.
5. Carrying out additional experiments for the generation of additional nano-catalysts for characterization via XAS to determine their reducibility in comparison to industrial catalysts.

3.2.3 Choice of the Characterization Methods

SEM was chosen for studying the particles morphology because the method generated images, allowing visual analysis of nano-scaled particles to develop qualitative conclusions. It was also possible to integrate the obtained SEM images in computations to develop quantitative measures of the morphological properties of the detected particles.

EDXS was employed for studying the composition. The method was time-efficient and detected composites with significant amounts, making it suitable for this purpose.

XAS was applied to understand the reducibility of the generated nano-catalysts. The method is suitable to detect whether a significant element reduction took place. This is because clear changes in the XAS spectra could be seen when changes in the oxidation states of a chemical element occur during its oxidation/reduction.

Chapter 4: Method

In the following sections, the materials, the completed experiments, as well as the analysis and characterization steps are described in detail.

4.1 Materials

The materials that were used in the experiments were Ni_3Mo_7 and Mo electrodes, purchased from Goodfellow Cambridge Limited. The carrier gas was nitrogen and it was a House gas. The SiOx wafers that were used as substrates for depositing the nanoparticles were obtained from SIEGERT WAFER.

4.2 Experimental Procedure

The following steps were carried out in each experiment.

1. The SDG chamber was mounted with the desired electrodes.
2. The system was then turned on, together with the connected LabView software.
3. The system was then vacuum pumped and monitored for a few minutes to ensure that there was no into-system air leak. During this time, the particle counter and the deposition chamber were off.
4. The gas couplings, pump, furnace, DMAs, as well as the particle counter, were then turned on.
5. The system parameters (constant and varied) were set (either through the software or locally) as desired for each experiment. The experiments that were carried out, together with their parameter specifications, are listed in Table 2 below.
6. When the furnace temperature reached the desired one, the flame was put on and the particle generation was initiated. The particle generation was then monitoring through the readings of the particle count.
7. The system was then observed for a few minutes to ensure its stability in terms of pressure, particle count, etc.
8. Once judged stable, the SiOx substrate was placed inside the deposition chamber, which was then vacuumed.
9. The desired depositing voltage was then applied, and the deposition was started and continued for a pre-determined period, based on the desired coverage. The deposition was continued for as long as required to achieve the physical coverage on the desired substrate as mentioned in point 9. The coverage time was determined by a calculation that considers the particle count reading, particle size setting of DMA2, the depositing voltage and the required particle density per cm^3 of the substrate. For this calculation, a function developed by PhD Calle Preger was used.
10. During each experiment, the discharge voltage reading was monitored, and the inter-electrode gap was manually adjusted accordingly, ensuring that the discharge voltage reading is maintained as desired.

11. Once the nanoparticle deposition was completed, the SiOx substrate with the deposited nanoparticles was taken out from the deposition chamber for characterization.

Table 2. List over the experiments that were carried out to study the size, shape and composition of the nanoparticles. Exp stands for Experiment, E electrode combination, V_d depositing voltage, F carrier gas flowrate through the SDG chamber, D depositing voltage and n DMAs. Experiments through which different levels of the same variable were investigated are marked with a matching colour of the cell of the investigated parameter. Experiments with the superscript 'EC' were used in the composition analysis, while those with the superscript 'A' were used for the additional XAS nano-catalyst characterisation.

Exp	E[*]	V_d (kV)	F (L/min)	T (°C)	D (kV)	n	Size through DMA2 (nm)	Coverage (%)
1 [E,1. n,1]	0	2.5	1.68	1200	7	1	12	3.0
2 [E,1. D,1]	1	2.5	1.68	1200	7	1	12	2.3
3 [V,1. F,2]	1	1.4	1.68	1000	7	2	12	27.0
4 [V,1. F,1. T,1]	1	2.5	1.68	1000	7	2	12	22.0
5 [V,2. F,2]	1	1.4	4.00	1000	7	2	12	22.6
6 [V,2. F,1]	1	2.5	4.00	1000	7	2	12	22.6
7 [T,1]	1	2.5	1.68	1200	7	2	12	2.3
8 [D,1. n,2]	1	2.5	1.68	1200	4	1	12	2.3
9 [n,1]	0	2.5	1.68	1200	7	2	12	3.0
10 [n,2]	1	2.5	1.68	1200	4	2	12	2.3
11 [EC]	0	2.5	1.68	1200	7	1	20	40.0
12 [EC]	1	2.5	1.68	1200	7	1	20	55.0
13-14 [A]	1	2.5	1.68	1200	7	1	20	87

[*] *0 is NiMo-Mo. 1 is NiMo-NiMo.*

[letter, number] *The letter superscript on each Exp are an extra indication of the variable for which the experiment was investigated. Experiments with the same number superscript were compared to each other. The superscript letters and the variables they stand for are E different electrodes, V discharge voltage, F carrier gas flowrate, T furnace temperature, D depositing voltage and n number of DMAs. EC stands for the variable different electrodes (E) in the composition experiments (C). A stands for the additional characterizations.*

4.3 Characterization and Analysis

SEM, EDXS and XAS were applied for the nano-catalysts characterizations as explained earlier. The names/sources of the devices, measurement parameters and characterized features are listed in Table 3 below.

Table 3. Characterization techniques, device names/sources and characterized properties.

Technique	Device name/source	Applied analysis parameters	Characterized properties
SEM**	Fei FibSEM, Lund Nano Lab	-Accelerating voltage 5 or 10 kV - Probing Current 98 μA, 25 pA or 0.13 nA.	-Sphericity -Agglomeration -Diameter* -Compaction* -Coverage*
EDXS**	JSM-6700F, Lund University	-20 keV maximum energy. -Line types: k for Ni and L for Mo.	Atomic composition Ni:Mo
XAS**	Balder beamline, MAX IV	XANES** -Ni: 8320-8390 keV -Mo: 19980-20080 keV	Oxidation/reduction

Calculations completed in MATLAB using the SEM images (see 4.3.1).

**SEM, EDXS, XAS and XANES stand for Scanning Electron Microscopy, Energy Dispersive X-ray Spectroscopy, X-ray Absorption Spectroscopy respective X-ray Absorption Near-Edge Spectroscopy.*

The characterization steps were started by the SEM measurements on samples 1-10 (Table 2), giving SEM images with a 2-dimensional projection of the 3-dimensional particles. These images were firstly examined visually to assess the sphericity and agglomeration of the particles qualitatively. Sphericity, in this case, is non-agglomerated round particle. Following this, sample images with visually acceptable spherical particles were identified and used in the further computational analysis to produce quantitative indications of the sphericity (roundness), particle diameters, compaction and coverage. For the other samples with aspherical and/or agglomerated particles, only the compaction and the coverage were computed. The particle sizes, in terms of diameters, were not computed as these were irrelevant for the agglomerated and aspherical particles. These computations were completed in MATLAB and are described in section 4.3.1 below.

For the compositional analysis, EDXS measurements on the samples that were obtained from experiments 11 and 12 (Table 2) were carried out, yielding the Ni:Mo atomic ratios. Five samples were obtained from each experiment, allowing the calculation of an average value for the composition of the particles.

Finally, XAS measurements were carried out on additional samples to deduce the oxidation and reduction properties of the nano-catalysts. This was done by obtaining X-ray Absorption Near Edge Spectra (XANES) during firstly oxidation, then reduction. For the oxidation step, the temperature was ramped from room temperature (RT) to 700 °C or 800 °C for Ni respective Mo under the flow of O_2 gas at atmospheric pressure (referred to as the oxidative gas). Following this, the reduction was an isothermal one at 700 °C or 800 °C for Ni respective Mo, and it was initiated by shifting to a 5 % H_2 in N_2 gas flow at atmospheric pressure (referred to as the reductive gas).

The first step of oxidation under temperature ramping was carried out to ensure that the Ni and Mo in the nano-catalyst were fully oxidized at the start of the reduction step. XANES from reference industrial catalysts were similarly obtained during reduction (no oxidation). These reference catalysts were prepared from powder catalysts and pressed into alumina.

To sum up, the steps that were followed during the characterization and analysis are summarized in Figure 3.
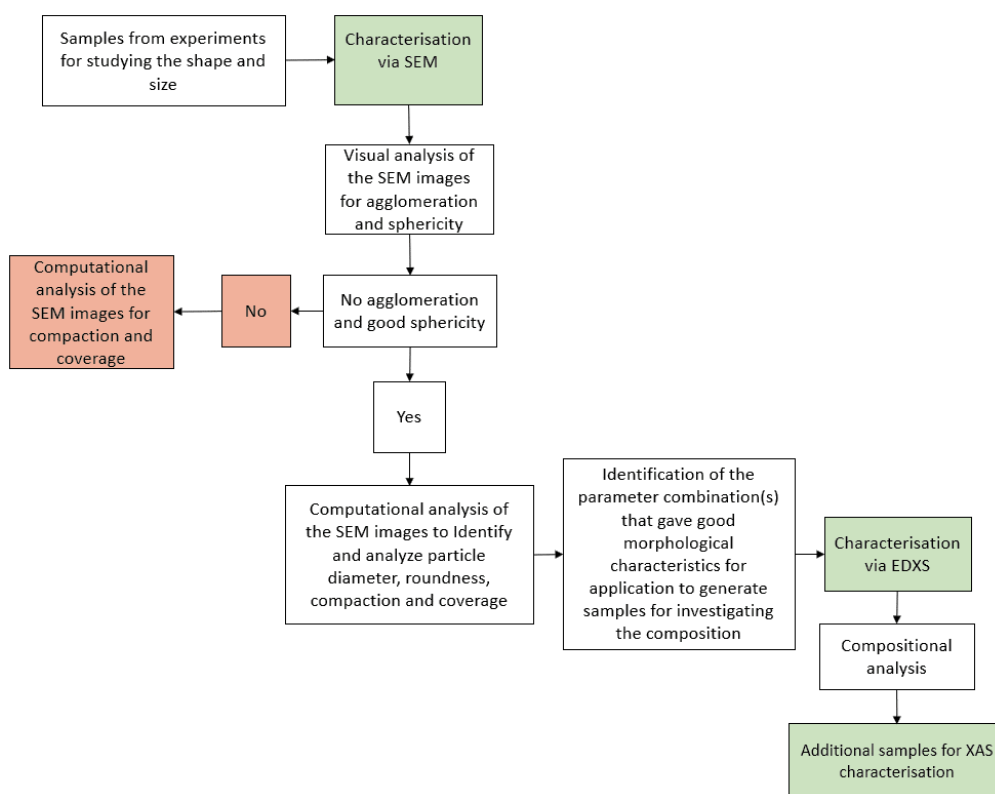

Figure 3. A summary of the steps that were followed during the analysis and characterization of the nanoparticles.

The computational analysis that was carried out on the SEM images is presented in the following section.

4.3.1 Computation of the SEM Images

The MATLAB computations of the SEM images were mainly completed by employing image segmentation techniques such that each SEM image was segmented into a background segment (defined as the dark gray shades in the image) and a particles segment (light grey shades). This segmentation was done by introducing a threshold value in the gray scale for each image, indicating a boundary between the two segments. The parts of the image that were defined as particles (particles segment) were then outlined and labelled, allowing the computation of the coverage, compaction, and diameter, as well as roundness metric of each identified particle.

4.3.1.1 Coverage

The (computational) coverage is mainly the ratio between the sum of the areas of the detected particles and the detected substrate area. This is to be viewed as an indication of the 'concentration' of the particles on the substrate. The coverages were calculated for each sample using the ratio between the sum of the areas of the identified particles and the total area of the images as presented in equation 6.

$$Coverage = \frac{\sum_{i=1}^{n} A_{pixel,i,j}}{A_{pixel,j}} \qquad (6)$$

$A_{pixel,i,j}$ is the area of particle i in image j in pixels. $A_{pixel,j}$ is the total pixel area of image j.

Coverage values were also generated during the experiments, using the particle count. These were used to determine the deposition period as was previously described. However, the computed coverage and the particle count-based coverage are not similar. Through the computational coverage, the detected particles and substrate areas were considered, while through the particle count-based coverage, the particles that were assumed to have been deposited onto a specified deposition area were considered.

4.3.1.4 Particle Compaction

The compaction revealed how compacted the identified particles were. For computing this, the SEM images were firstly converted into binary images (black and white). Corresponding images to these were then synthesized with hole-filled particle segments. A 'hole' in this case refers to a region, within an identified particle boundary, with pixel characteristics that match those of the background pixels (i.e. small black region within a white 'particle' one). Thus, hole-filling refers to filling up these 'gaps' by converting any black background-segment-matching pixels within the boundaries of an identified particle to white particle-segment-matching pixels. This is depicted in Figure 4, where an original hole-unfilled binary image was transferred to a hole filled binary image.
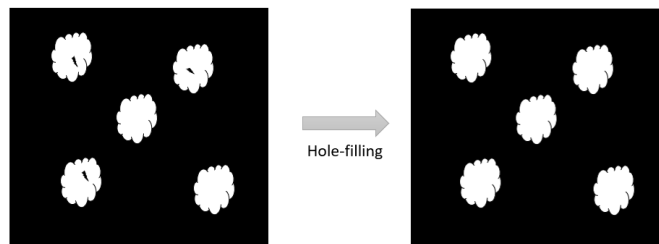
Figure 4. Demonstration of hole-filling in binary images. The white regions are the identified particle segment and the black region is the background segment.

As can be seen in Figure 4, hole-filling, in this case, increases the overall number of white regions in the image, meaning that the white pixels increase in number. Thus, to deduce the particle compaction, the number of white pixels in the hole-unfilled binary image was compared to that in the corresponding hole-filled binary image using equation 7.

$$Compaction = \frac{number\ of\ white\ pixels\ in\ the\ unfilled\ binary\ image}{number\ of\ white\ pixels\ in\ the\ filled\ binary\ image} \quad (7)$$

A value of 1 indicated excellent compaction, i.e. there were no 'holes' in the hole-unfilled binary image. A value of less than 1 indicated that compaction was possibly imperfect.

4.3.1.3 Particle Size: Diameter

Using the counted areas (in pixels) of the identified particles in each SEM image, the mean diameter was simply approximated using equation 8.

$$\overline{d_{i,J}} = \overline{\sqrt{\frac{4*A_{i,J}}{\pi}}} \quad (8)$$

$d_{i,j}$ is the diameter of particle i in image j, where image j is one with particles that have considerably low agglomeration level and good sphericity, based on the visual analysis. Note that particle i is assumed to be spherical. $\overline{d_{i,J}}$ is the mean diameter of the articles in image j. $A_{i,j}$ is the area of the particle. The original dimension of the calculated $d_{i,j}$ values was in pixels but these were converted to nm using a conversion factor that was derived from the nm scale provided in the SEM images and a length matching pixel scale generated in MATLAB.

4.3.1.4 Roundness Metric

A mean roundness value, indicating the average sphericity of the identified particles in each SEM image, was computed using the perimeter and the area values of the particles. This was performed to facilitate the comparison between samples with visually identified spherical particles. The mean roundness matric was calculated as shown in equation 9.

$$\overline{Roundness\ matric} = \overline{\frac{2*\pi*A_{i,j}}{P_{i,J}{}^2}} \quad (9)$$

$A_{i,j}$ is again the area of particle i in image j that has detected particles with no agglomeration and good sphericity. $P_{i,j}$ is the particle's perimeter. Mathematically, the roundness metric is equivalent to 1 for perfectly round objects, which are considered perfectly spherical.

Chapter 5: Results and Discussion

In this chapter, the results that were obtained from the SEM, EDXS and XAS characterizations are presented and discussed.

In section 5.1, the qualitative and quantitative analysis of the SEM images is presented. In section 5.2, the results from the EDXS measurement showing the different particle compositions are presented. Finally, in section 5.3, the results that were obtained from the XAS measurements showing the oxidation and reduction properties of the NiMo nanoparticles are presented.

5.1 Shape and Size

In the sub-section 5.1.1, all the studied SEM images are presented, with the corresponding qualitative observations and pairwise comparisons that were made through the visual analysis. The pairs of images that were compared are described in Table 2. The coverage and compaction values are also presented for each of the SEM images. In the sub-section 5.1.2, the mean diameter and roundness metric values are presented for each of the SEM images with non-agglomerated, spherical nanoparticles.

5.1.1 Visual Analysis: Agglomeration and Sphericity

The SEM images that were obtained from experiments 1-10 (Table 2) are presented in Figure 5. SEM images obtained at a lower magnification (80 000x) are also presented in Appendix II. The coverage and particle compaction in the SEM images were also calculated using equations 6 and 7, and these are presented in Figure 6.
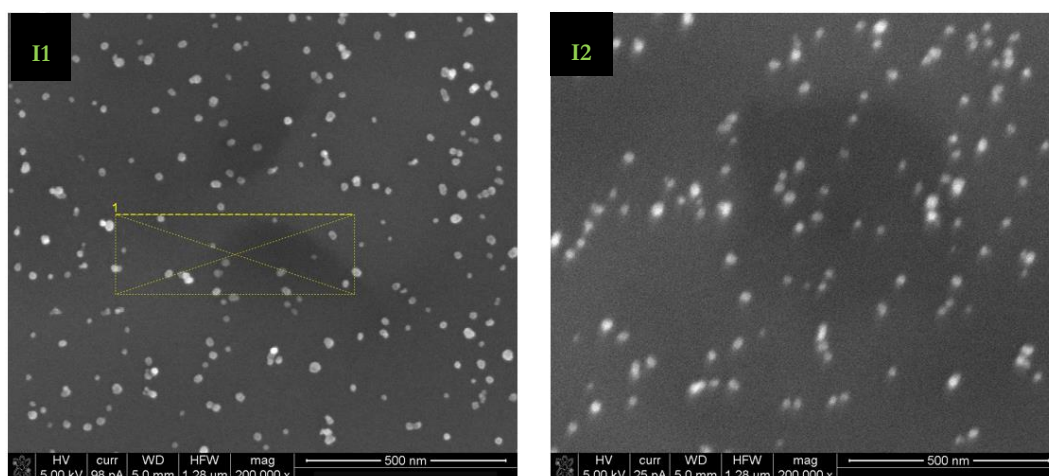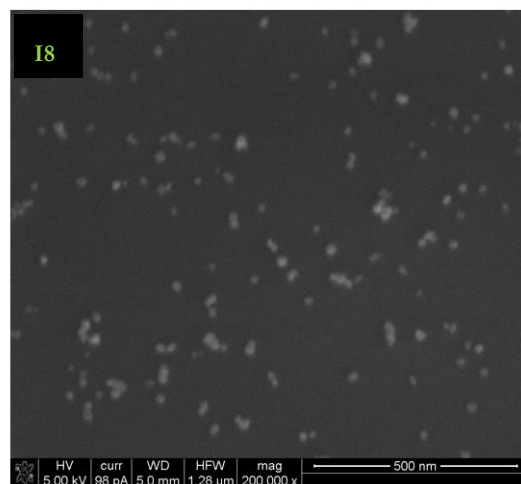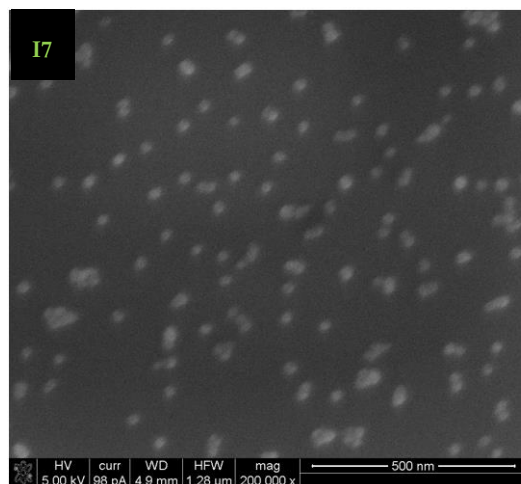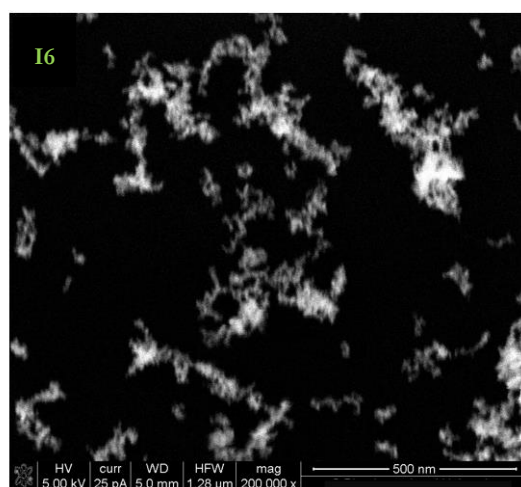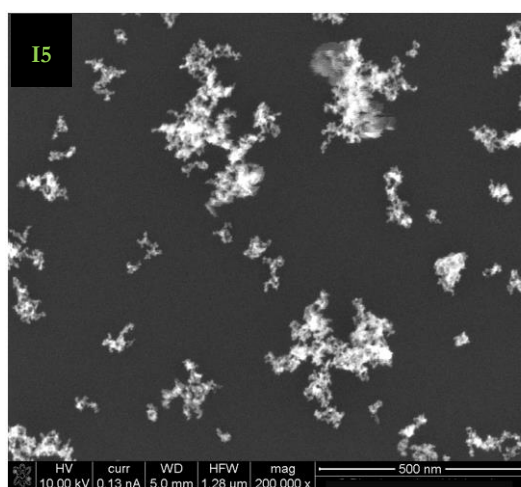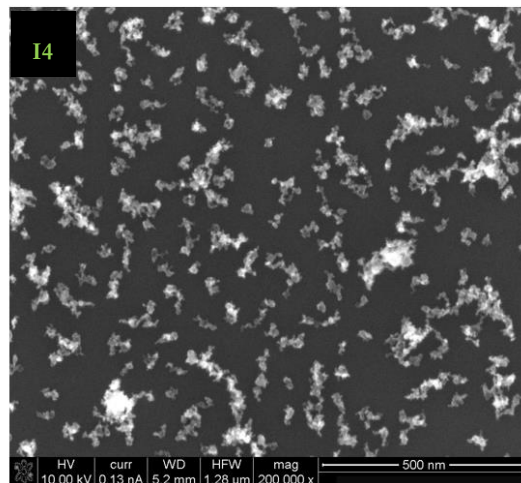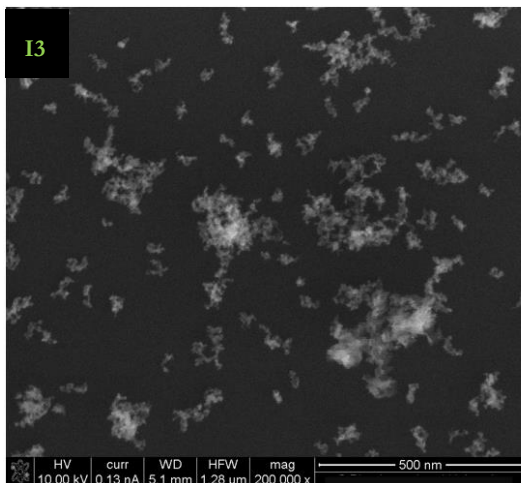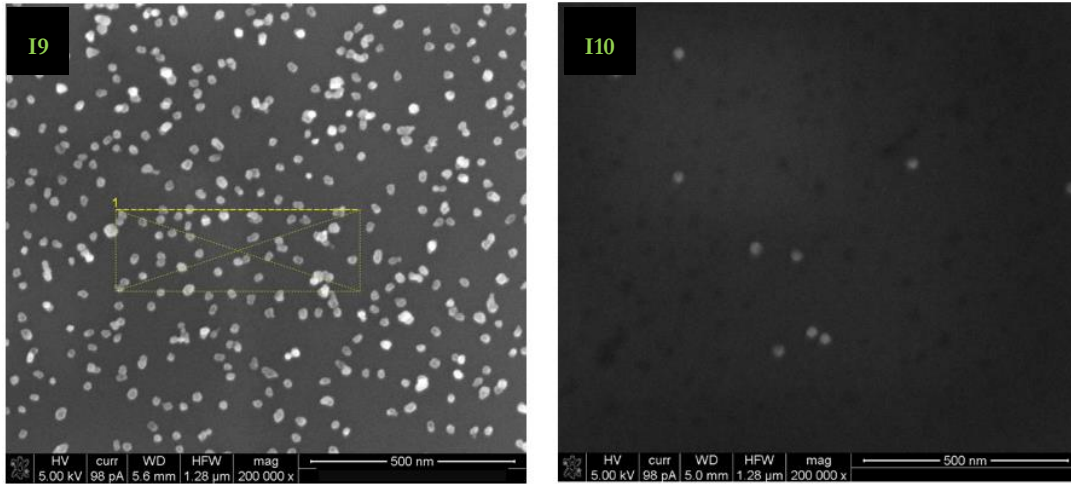
Figure 5. SEM images for experiments 1-10. 'I' beside the experiment number stands for Image.
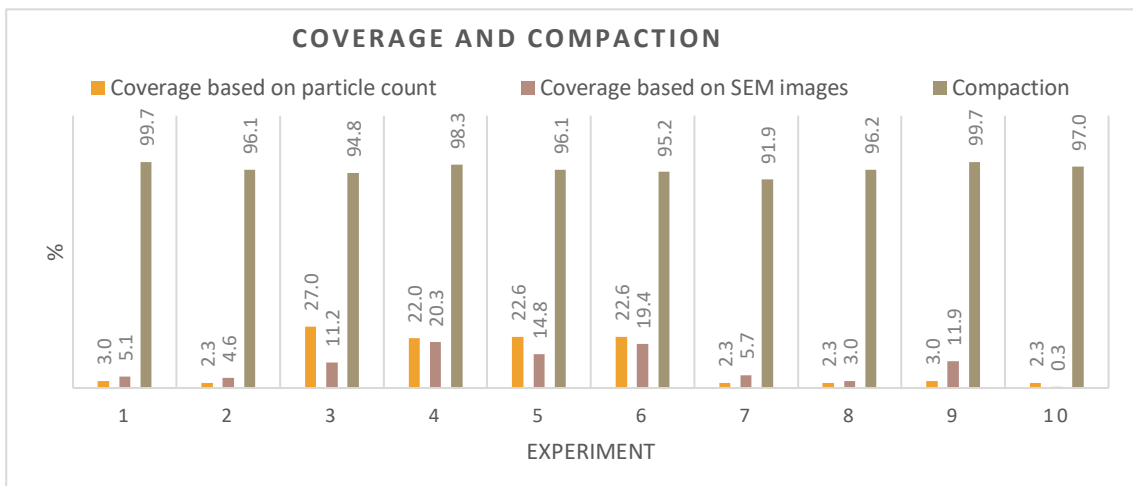
Figure 6. The computed Coverage and Particle Compaction values of the nano-catalysts using SEM images obtained at 200,000x magnification, together with the particle count-based coverage values.

Based on Figure 5, generally well distributed particles were yielded. This was also noticed in the SEM images that were obtained at 80,000x magnification (Appendix II). Through the visual analysis and pairwise comparison of the SEM images, the effect of the different levels of the independent variables (Table 1) on the particle agglomeration and sphericity was observed. The observations were as follows.

o Non-agglomerated, spherical particles were obtained using both NiMo-Mo and NiMo-NiMo electrode combinations, as was revealed by comparing I1 (NiMo-Mo) and I2 (NiMo-NiMo).

o At both tested discharge voltage levels (1.4 or 2.5 kV), agglomeration was obtained as revealed by considering I3 and I5 (1.4 kV) in comparison with I4 and I6 (2.5 kV). That is, changing the discharge voltage at the tested levels resulted in no elimination of the particle agglomeration/sphericity. However, the agglomerates that were obtained using 2.5 kV show an elongation characteristic and less branching than those obtained at 1.4 kV.

o Agglomeration was also yielded at both carrier gas flowrate levels (1.68 L/min or 4.00 L/min), as shown in I3 and I4 (1.68 L/min) compared to I5 respective I6 (4.00 L/min). Moreover,

26

larger and/or more branched agglomerates are present in the images of the samples where 4.00 L/min was employed (I5 and I6).

o Increasing the furnace temperature from 1000 °C to 1200 °C eliminated agglomeration and yielded spherical particles, which was observed upon comparing I4 (1000 °C) with I7 (1200 °C). Also, considering all of the experiments simultaneously, agglomeration was obtained whenever 1000 °C was employed in the furnace (I3-I6), while non-agglomerated particles were detected in all experiments where 1200 °C was employed.

o At any of the tested depositing voltage levels (4 or 7 kV), non-agglomerated nanoparticles were detected, as could be seen by considering I8 (4 kV) and I2 (7 kV). Thus, no statement on how changing the depositing voltage at the tested levels could affect the particle sphericity or agglomeration could be made.

o No effect on the particle sphericity or agglomeration properties could be detected upon employing 1 or 2 DMAs as non-agglomerated, spherical nanoparticles were yielded at both levels. This could be seen by comparing I1 and I8 (2 DMAs) against I9 and I10 (1 DMA).

By examining the coverage and compaction values in Figure 6, the following points were identified.

o The particle count-based and SEM image-based coverage values are not similar in each experiment and do not show similar trends. Experiments 3, 4, 5 and 6 have significantly higher coverage values (both particle count-based and computational) than the rest.

o The compaction values vary among the different experiments. The highest compaction, 99.7 %, corresponds to experiments 1 and 9. The lowest compaction is 91.9 % and it corresponds to experiment 7.

By considering the observed effect of the electrode combination on the level of nanoparticle agglomeration, no special trends could be detected. Besides, using the same combination of NiMo-NiMo, agglomerated, and non-agglomerated nanoparticles were yielded (see I2 and I3). This implies that obtaining agglomeration or not, is not necessarily a direct consequence of employing one specific electrode combination.

Neither changing the discharge voltage nor the gas flowrate through the SDG chamber resulted in eliminating agglomeration. An important factor to consider is that the experiments that were considered for studying the effect of these parameter (I3-I6 in Figure 5) were completed at 1000 °C furnace temperature, and no non-agglomerated particles could be yielded at this temperature as reported above. Thus, this employed temperature level could have been the main factor that most strongly enhanced the agglomeration of the particles at any of the tested depositing voltage and gas flowrate levels.
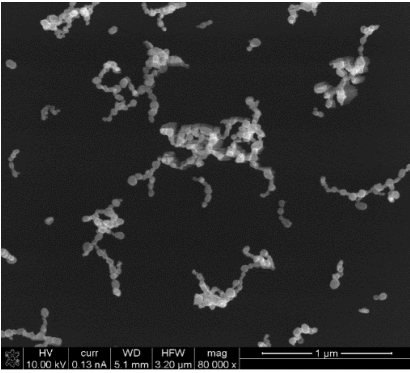
Figure 7. Ni nanoparticles generated via SDG.

Yet, an interesting observation was that at 2.5 kV, compared to 1.4 kV discharge voltage, more expanded agglomerates with less branching were obtained. This could be related to that increasing the discharge voltage increases the spark energy as demonstrated by equation 1 [11], making more energy available for a higher level of electrode material evaporation. At a higher evaporation level, a higher Ni amount, as well as Mo, would be yielded. Increasing the amount of Ni among the yielded nanoparticles was found to affect their morphology. Ni is one of the naturally occurring magnetic elements and in one study targeting the impact of Ni magnetization on the shape of Ni nanoparticle-based nanotruss, increasing the Ni amount led to increasing the synthesized truss lengths and decreased branching [16]. That is, the observed decrease in the branching of the agglomerates at 2.5 kV discharge voltage might have occurred due to a higher amount of magnetic Ni because of higher spark energy and electrode evaporation. To visualize the magnetization of Ni, an SEM image of supported SDG Ni nanoparticles, generated by employing two Ni electrodes, was obtained and is presented in Figure 7, where the magnetic character of the Ni is clearly detectable through the lining and branching in the nanoparticle chains.

By considering the effect of the carrier gas flowrate on the nanoparticles, agglomeration was not eliminated upon increasing the flowrate through the SDG as was described above. This violates previously reported findings, where increasing the flowrate through the SDG chamber was correlated to a reduction in the sizes of the particles [3]. However, the obtained results could be due to the experimental system setup. As explained earlier, different flowrates were employed through the SDG and through the rest of the system. This was the case for 4.00 L/min flowrate, which was only employed through the SDG chamber, while 1.68 L/min through the rest of the system. This could have affected the particle morphology. To further develop this discussion, equation 5 could be considered: increasing the flowrate through the SDG chamber would decrease the mean particle diameter (size) due to the resulting cooling and dilution effect on the synthesis region [3, 14]. Employing 4.00 L/min through the SDG chamber might have actually enhanced the generation of small and non-agglomerated particles in accordance to equation 5, but these were carried at a much slower flowrate of 1.68 L/min after exiting the SDG chamber. This means more time and probability for the particles to accumulate and undergo agglomeration after the SDG chamber, resulting in the detected agglomeration. As this might be the explanation, it remains uncertain and an experimental design that facilitates yielding and comparing nanoparticles after different units, for example after the SDG chamber and after the furnace, should be implemented to help demonstrate this.

Increasing the furnace temperature from 1000 to 1200 °C eliminated agglomeration and enhanced the sphericity of the nanoparticles. In the reviewed theory, increasing the sintering temperature of the SDG-nanoparticles also decreased the sizes of the agglomerates and improved the particle sphericity [6], [14], which generally agrees with the findings of this study.

Non-agglomerated and generally spherical nanoparticles were also obtained at either 4 or 7 kV depositing voltage. However, in some of the experiments where 7 kV was employed, agglomeration was obtained. This implies that the depositing voltage level does not necessarily impose an effect on the nanoparticles and that other parameters, possibly but not necessarily in combination with the discharge voltage, affected the morphology of the particles more significantly. The same applies for applying 1 or 2 DMAs, as no direct effect on the level of the particle agglomeration could be seen.

Considering the coverage values, comparing the particle count-based (connected to the coverage time during the experiments) and the SEM image-based ones revealed discrepancies between the two measurements in all experiments. This is likely due to misestimations and/or oscillations in the readings of the particle count by the particle counter device, leading to choosing an unrepresentative particle count value for the calculation through which the particle count-based coverage values were deduced. The oscillations in the particle count reading are further discussed in sub-section 5.2.

One noted trend was however that the coverage values corresponding to experiments 3, 4, 5 and 6 are the highest, simultaneously with these experiments having the highest levels of particle agglomeration (Figure 5 and 6). The intended coverage could have impacted the dispersion and distribution of the particles on the substrates as higher coverage/ longer coverage time meant more nanoparticles being deposited on the substrate, and this might have enhanced agglomeration. However, even though this is possible, it is not necessary as the observed agglomeration could also be correlated to other system parameters (mainly furnace temperature), as was discussed above.

Regarding the compaction, different values were obtained, and those for experiments 1 and 9 were the highest. Interestingly, these experiments gave particles with high and statistically similar mean roundness metrics. This will be further discussed in sub-section 5.1.2, where the results of the particle sizes and roundness metrics are presented.

In general terms, throughout the qualitative analysis of the SEM images, the terms non-agglomeration and sphericity were often related. Obtaining spherical particles and agglomerated ones is not necessarily mutually exclusive as noted from previously reported results in morphological terms in other studies. However, as agglomerated spherical particles would not either be interesting as model catalysts, any agglomerated particles were excluded and assumed aspherical.

An important notice to bear in mind is that the collected data is a simplification of the real-life model catalysts and the detected properties are also a simplification. The SEM images show 2D projections of 3D particles. All the detected particles in the SEM images were treated as separate particles on the support plane. However, it is very likely that particle growth perpendicular to the support plane had occurred. This can possibly explain the presence of different particle brightness

levels in the same image (see I4 and I9 in Figure 5), where the brighter appearing particles are furthest away from the support plane. However, whether out-of-plane particle growths have occurred or not, could not be determined, and further SEM characterizations with the electrons ejected parallelly to the support surface can reveal such morphological trends.

In summary, the qualitative results show that low to no agglomeration and good sphericity were obtained when employing NiMo-NiMo or NiMo-Mo electrode types/combination, 1200 °C furnace temperatures, 4 or 7 kV depositing voltage and/or using 1 or 2 DMAs. Variable coverages and compaction values were obtained, where the highest coverages were obtained from the experiments with the highest level of agglomeration. The highest compaction was 99.7 %. Table 4 below lists the pairwise compared experiments/SEM images in relation to the examined independent variables, the observed agglomeration and particle sphericity trends, the coverage and compaction values

Table 4. Summary of Visual Analysis of the SEM images together with the coverage and compaction values.

Variable	Experiment (tested level)	Agglomeration (and aspherical)	Identified trends: variable, agglomeration, sphericity	SEM-based Coverage (%)	SEM-based Compaction (%)
Electrodes (E)	1 (NiMo-Mo)	No	None. Low agglomeration and spherical particles obtained at all levels.	5.1	99.7
	2 (NiMo-NiMo)	No		27.0	96.1
Discharge Voltage (V$_d$) *And* Carrier gas flowrate through the SDG chamber (F)	3*,*** (1.2 kV) (1.68 L/min)	Yes	None. Agglomeration obtained at all levels.	11.2	94.8
	4*,**** (2.5 kV) (1.68 L/min)	Yes		20.3	98.3
	5**,*** (1.4 kV) (4.00 L/min)	Yes		14.8	96.1
	6**,****	Yes		19.4	95.2

	(2.5kV) (4.00 L/min)*				
Furnace Temperature (T)	4 (1000 °C)	Yes	Agglomeration decreased and sphericity increased with increasing temperature	20.3	98.3
	7 (1200 °C)	No		5.7	91.9
Depositing Voltage (V)	8 (4 kV)	No	None. No agglomeration and spherical particles obtained at all levels	3.0	96.2
	2 (7 kV)	No		4.6	96.1
Number of DMAs (n)	1**** (1 DMA)	No	None. No agglomeration and spherical particles obtained at all levels	5.1	99.7
	9**** (2 DMAs)	No		11.9	99.7
	2***** (1 DMA)	No		4.6	96.1
	10***** (2 DMAs)	No		0.3	97.0

*/**/***/****/*****/*******Pairs of experiments marked with the same number of starts were compared against each other.*

5.1.2 Particle Sizes and Roundness metrics

The diameter and roundness metric computations were done on the SEM images with non-agglomerated and spherical particles, namely those from experiments 1, 2, 7, 8, 9 and 10, in accordance with the characterization plan. These were computed using equations 8 and 9, as described in Chapter 4. To present the data, roundness metric versus diameter scatter plots, as well as diameter distribution curves, were plotted and are presented in Figures 8-13, together with the segmented SEM images. Note that the scales in the y-axes are not similar among the figures. Corresponding distribution parameters, including the mean diameters and roundness metrics, are listed in Table 5.

Figure 8. Segmented SEM image with indicated boundaries (left). Diameter distribution and roundness metrics for I1 (right).

Figure 9. Segmented SEM image with indicated boundaries (left). Diameter distribution and roundness metrics for I2 (right).

Figure 10. Segmented SEM image with indicated boundaries (left). Diameter distribution and roundness metrics for I7 (right).
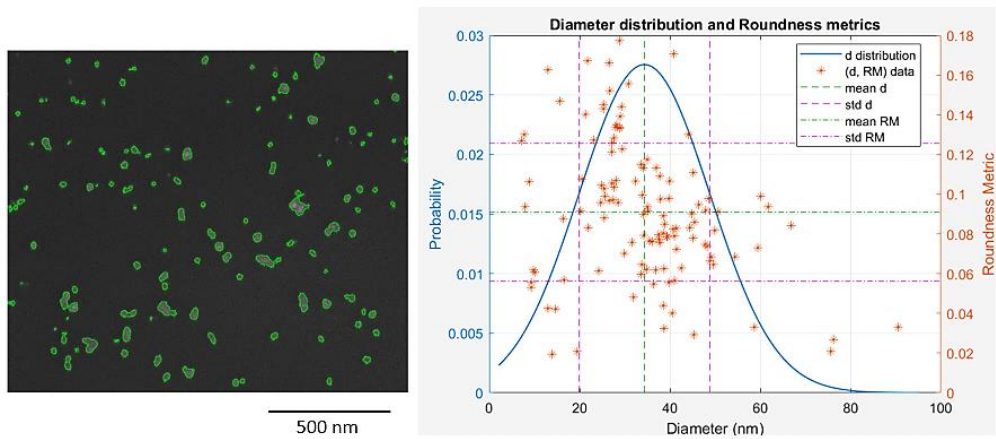
Figure 11. Segmented SEM image with indicated boundaries (left). Diameter distribution and roundness metrics for I8 (right).
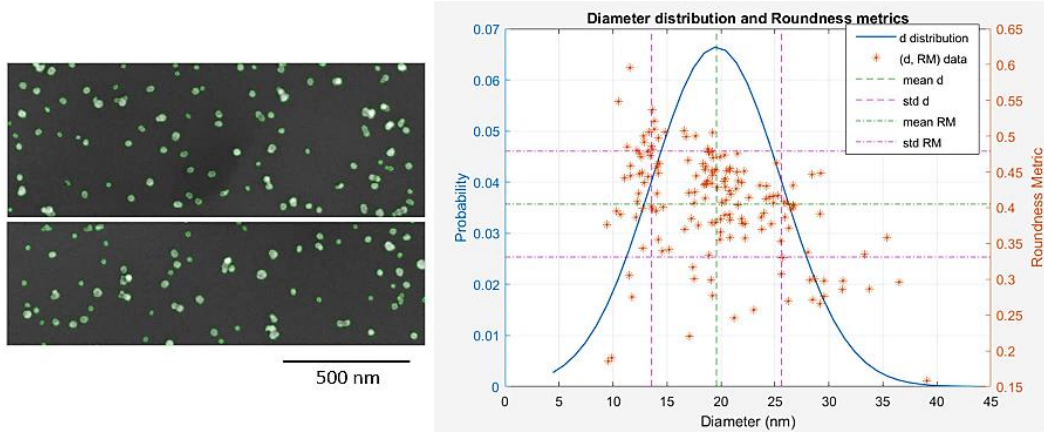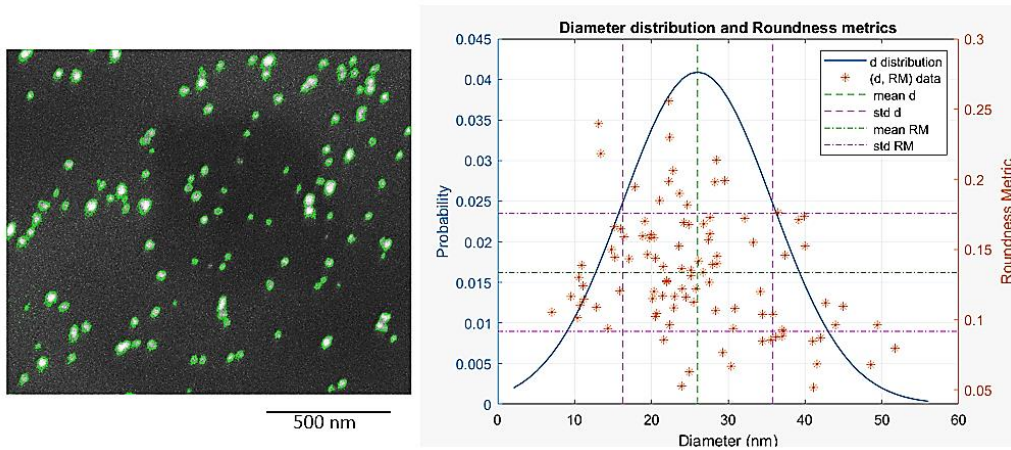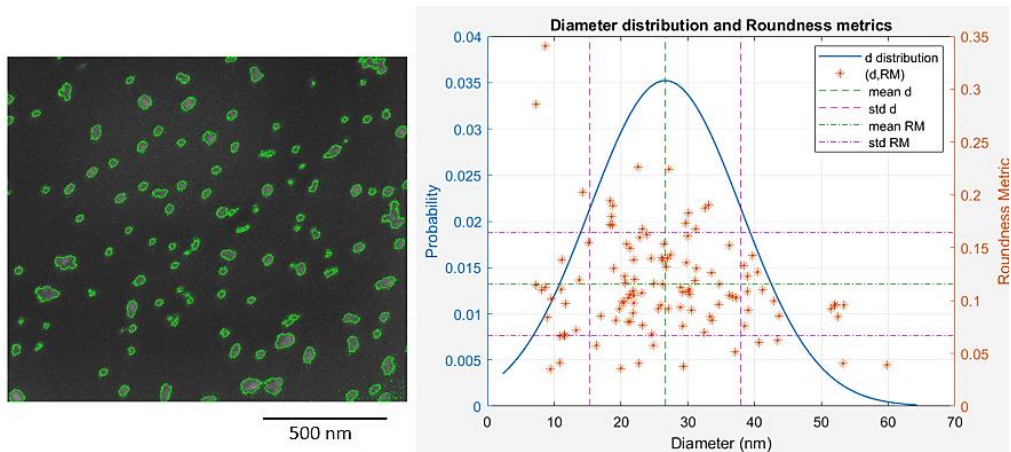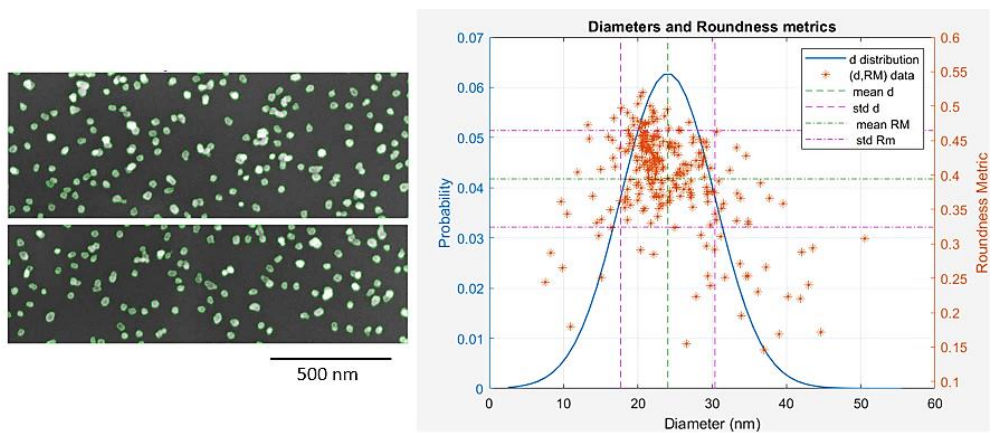

Figure 12. Segmented SEM image with indicated boundaries (left). Diameter distribution and roundness metrics for I9 (right).

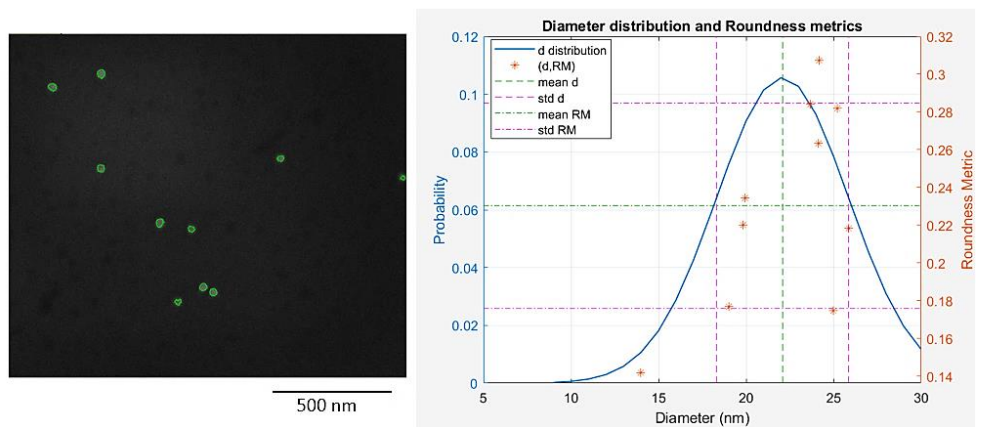*Figure 13. Segmented SEM image with indicated boundaries (left). Diameter distribution and roundness metrics for I10 (right).*

Based on the diameter distributions, the distribution broadness and mean values vary among the different experiments. To be able to clearly illustrate the relative difference between the distributions, a figure with all the distribution curves in the same plot is presented in Appendix III.

33

Table 5. The approximated mean diameters ($\bar{d}$), mean roundness metrics ($\overline{RM}$), diameter standard deviations (δ_d), roundness metric standard deviations (δ_{RM}), diameter intervals [d_{min},d_{max}] and roundness metrics intervals [RM_{min},RM_{max}] corresponding to Figures 8-13 for experiments 1, 2, 7, 8, 9 and 10.

Exp	$\bar{d}_{\pm \delta d}$ (nm)	[d_{min},d_{max}] (nm)	$\overline{RM} \pm \delta_{RM}$	[RM_{min},RM_{max}]
1	19.58 ± 6.01	[9.43, 39.10]	0.41 ± 0.07	[0.16, 0.60]
2	26.03 ± 9.75	[7.09, 51.70]	0.13 ± 0.04	[0.05, 0.26]
7	26.65 ± 11.32	[7.30, 59.78]	0.12 ± 0.05	[0.04, 0.34]
8	34.36 ± 14.48	[7.09, 90.55]	0.09 ± 0.03	[0.02, 0.18]
9	24.02 ± 6.35	[7.49, 50.51]	0.39 ± 0.07	[0.15, 0.52]
10	22.08 ± 3.77	[13.99, 25.88]	0.23 ± 0.05	[0.14, 0.31]

When comparing all the diameter distributions against each other, the following trends were identified.

- The smallest mean particle diameter that was obtained was approximately 19.58 nm in experiment 1 (Figure 8). The probability of getting a particle with this size was around 0.065. Notice that none of the mean diameter values was matching with the setting of the DMA2 (12 nm), which was the size selecting unit in these experiments.
- The largest mean particle diameter was 34.36 nm, which was obtained in experiment 8 (Figure 9) and the corresponding probability was about 0.028.
- The smallest detected particle was 7.09 nm from experiments 2 and 8, and the largest one was 90.55 nm from experiment 8 (Table 5).
- The narrowest distribution was that of experiment 10, followed by experiments 1 and 9. The broadest one was that of experiment 8 (Appendix III).
- Using 1 and 2 DMAs, as in I1 and I2 compared to I9 and I10, diameter distributions with similar broadness were obtained in one case, but a narrower distribution was obtained using 2 DMAs in the other case (Appendix III).
- The mean diameter values from experiments 2, 7, 9 and 10 were numerically close to each other but highly differ from those that were gotten in experiments 1 and 8.

When considering the roundness metrics, the following trends were identified

- o The highest mean roundness metric was 0.41 and this was obtained in experiment 1, in which the smallest mean particle diameter was yielded. The lowest roundness metric, 0.09, was obtained in experiment 8 (Table 5).
- o The standard deviations of the roundness metrics in all the experiments were around 0.03-0.05, except for experiments 1 and 9, which have the largest standard deviations of about 0.07.

In relation to the investigated variables, the obtained mean particle diameters were smaller, and the roundness metrics higher upon employing:

- o NiMo-Mo electrodes (experiment 1).
- o 7 kV as the depositing voltage (experiment 2).
- o 1 DMA based on the comparison between experiments 1 and 9, but 2 DMAs based on experiments 8 and 10.

19.58 nm was the smallest mean particle diameter that was obtained, which was not expected. Instead, mean particle diameters around 12 nm were expected because the DMA settings were adjusted to allow particles with sizes of 12 nm through. The reason for this is unclear, but it could be due to miscalibrations or malfunctioning in the DMAs. Another reason could be that the nanoparticles increased in size, for example via coagulation, past DMA2. However, as this remains uncertain, most of the obtained mean diameter values are reasonable. DMA1 was set to release particles with sizes of 35 nm and all the mean diameter values, including their standard deviations (Table 5), are within the interval of 12 nm and 35 nm. I8 was, however, an exception as it has a wide diameter distribution curve and a large standard deviation.

The probability of obtaining a particle with the size of 19.58 nm is 65 in 1000 nanoparticles, which is a low probability. The reason for this is unclear, but it is possible that nanoparticles were lost via adsorption onto the walls of the system, giving a low particle yield. This is very likely in the furnace where the temperature was 1200 °C. The smaller the particle dimensions are, the lower their melting points are. Thus, at the employed furnace temperatures, nanoparticle of the smallest dimensions might have melted and fouled onto the walls of the system.

When considering the broadness of the diameter distribution curves using 1 or 2 DMAs, the curves were similar in the first case, but different in the second. Obtaining similar distributions in the first case was not expected as using 1 DMA was expected to result in a broader size distribution due to more particles being released towards the deposition chamber. In the second case, obtaining a narrower distribution upon employing 2 DMAs is more reasonable. However, one of the experiments that were compared in the second case had low coverage (experiment 10 with only 10 particles). This limits the strength of its results as the low coverage implies that the considered datapoints are too few to assume that the conclusions from this experiment are trustworthy. To fully demonstrate the effect of the number of employed DMAs, more experiments are required. In these experiments, the effect of having different coverages must also be considered.

Some experiments have numerically close mean diameter values, as mentioned above. To examine whether these are statistically different or not, pairwise t-tests on the diameters were carried out. Ninety random particles were chosen from each experiment to complete the t-tests. The null hypothesis was that all the mean diameter values that are presented in Table 5 were statistically indifferent and the alternative hypothesis was that there was a significant difference between these at a significance level of 5 %. It was found that the only mean diameter values that were insignificantly different are those that were yielded for the experiment pairs 2 and 7, 2 and 9 and 7 and 9. The other pairs are statistically different. It must be noted that experiment 10 was not compared with any other experiment because of its low coverage, making the results statistically untrustworthy as all other images have much more nanoparticles (at least 100 detected nanoparticles).

Having statistically indifferent diameter values among some experiments indicates that the observed numerical differences among these are possibly due to random rather than due to manipulating the system parameters. It is also logical to consider that the parameters that were employed at different levels in these experiments are probably insignificant for the particle sizes since the statistical similarity was detected regardless the differences in these parameters among experiments 2, 7 and 9. The parameters that differed among the specified experiments were the electrode combination and number of employed DMAs in the system (Table 2). As an example, the electrode combination that was used in experiment 9 was different from those in experiments 2 and 7. Obtaining statistically similar mean diameters in experiments 2, 7 and 9, regardless of using different electrodes in these experiments could be an indication that the electrode type does not necessarily influence the sizes of the nanoparticles. Alternatively, a possible indication of this is that (one of) the parameters that were set at a similar level in all three experiments, which were the discharge voltage, the flowrate, the furnace temperature and depositing voltage, (was) were the most significant for determining the particle sizes.

A significant effect due to the combination of the electrodes on the mean particle diameters was, however, obtained upon comparing experiments 1 and 2 (considering Table 2, Table 5 and the t-tests). A smaller diameter was obtained using NiMo-Mo compared to NiMo-NiMo. This finding contradicts the previous discussion, and instead, it possibly implies that the electrodes type have a significant effect on the size of the particles. To further examine this, previously reviewed literature was considered, where the particle sizes were correlated to the physical properties of the electrodes. The yielded monometallic mean particle sizes were reported to have increased due to using electrode materials with higher ionization energies, while for bimetallic ones, the size distributions were between the monometallic distributions of the constituent metals [12]. Accepting this, Ni has higher ionization energy than Mo (Appendix I), meaning that if Ni monometallic nanoparticles were generated using Ni-Ni electrode combination, they would be larger than Mo monometallic nanoparticles that were generated from Mo-Mo electrodes. Meanwhile, if bimetallic nanoparticles were generated from a combination of Mo and Ni electrodes, their size distributions would fall between the two monometallic Ni and Mo nanoparticle size distributions. Relating this to the bimetallic NiMo nanoparticles that were generated in this study, replacing one NiMo electrode with

36

Mo, which has lower ionization energy than Ni, might have been a cause to the detected decrease in the mean sizes of the nanoparticles as the particle size reduction effect is enhanced using a pure Mo. This provides a reasonable explanation to why the electrode types could affect the sizes of the yielded nanoparticles. Reconsidering the previously discussed case, where a statistically similar diameter was obtained in experiments 2, 7 and 9 regardless employing different electrode combinations among the experiments, obtaining indifferent particle sizes could instead be explained in terms of the employed parameters in combination rather than one separate parameter, the electrodes type.

Pairwise t-tests were also carried out to assess which of the mean roundness metrics are significantly different at 5 % significance level, and these revealed that all of the roundness metrics that are presented in Table 5 are significantly different, except for those of experiments 1 and 9. In these experiments, the effect of using 1 or 2 DMAs was studied, and this t-test reveals that different number of DMAs did not necessarily influence the roundness of the particles.

However, for experiments 1 and 9, the obtained results in terms of the roundness metrics and t-test were considered together with the compaction results (5.1.1). It was deduced that high and similar roundness metrics, as well as high compaction values were obtained simultaneously in these experiments. Thus, the compaction of the nanoparticles is likely related to their roundness metric. This is reasonable as the more spherical a geometrical shape is, the more likely it is that its volume is effectively packed. Besides, the particle sizes that were obtained in experiments 1 and 9 are relatively small, which could also indicate that this latter variable is related to the other two. To certainly demonstrate this, more studies of the geometrical properties of the nanoparticles must be carried out.

When considering both the diameter and roundness metric results, outliers were spotted in the data plots in Figure 8-13. To suitably examine these, box and whisker plots were constructed and are presented in Figure 14. Note that the y-axes are not on the same scale.
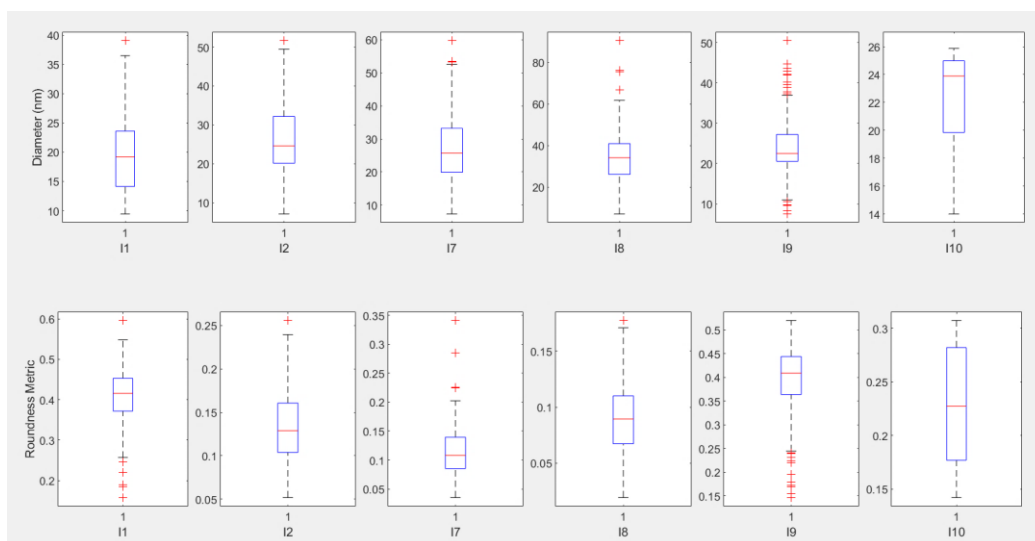

Figure 14. Boxplot for the Diameters and Roundness metrics showing the outliers marked in red.

As shown in Figure 14, the outliers are either occurring with respect to the diameter, the roundness metrics or both. I10 has no outliers with respect to neither the diameter nor the roundness metrics. I2 has one outlier with respect to both diameter and roundness metric. The experiment that has the most outliers, both with respect to the diameter and the roundness metrics, is experiment 9. The broadness of the experimental data could also be deduced by considering the length of the boxes (note that the y-axes are not similarly scaled).

Even though outliers in the data points with respect to the diameter values and/or roundness metrics were detected, these outliers were not removed. This was because these were often outliers with respect to only one of the two variables mean diameters and roundness metrics. Removing data points that were outliers with respect to one of these would have meant removing datapoints that were valid with respect to the other variable. It was also thought that excluding outliers, in this case, would correspond to excluding features from the image. The outliers did not represent normative features among the detected nanoparticles, but they were a consequence of the system synthesis, as well as the characterization and computational methods.

For example, in I2, there was one particle that was an outlier with respect to the particle diameter (Figure 14). Investigating the nanoparticles in I2 revealed that there were two nanoparticles that were deposited very close to each other. In the MATLAB computations, these two particles were not resolved and instead identified as one data point with a large mean diameter. Eliminating this data point, in this case, would have masked the fact that some particles could undergo a form of clustering, even though overall clustering was not the common trend in this sample. Besides, excluding such a data point would have also masked over the fact that the adopted computational methods could not resolve or identify such trends. This is partly because of the thresholding. For this case, the resolution could have eventually occurred by increasing the threshold value, but this would have occurred in the expense of making the particles appear smaller than they probably are since the segmentation boundaries would have contracted.

Regarding the effect of the furnace temperature on the particle sizes and roundness, all the samples that are presented in Table 5 were synthesized at 1200 °C. Thus, no relation in terms of changes in the mean particle size or the mean roundness metrics with the furnace temperature was identifiable. However, at this temperature, variable mean particle diameters and roundness metrics were obtained; (Table 5). This possibly implies that other parameters were probably affecting the nanoparticle characteristics at this temperature level. However, since no agglomeration was obtained in any of the experiments that were completed at 1200 °C, as described above, the effect of the higher furnace temperature on eliminating agglomeration is probably very significant, regardless the variation particle sphericity (roundness metric) and size.

For the discharge voltage and carrier gas flowrate, no result statements could be made in terms of how the mean particle diameter or the mean roundness metrics were affected by changes in the

these as agglomeration was obtained in all of the experiments that were studied for these variables (Table 4), and thus no further computation of the corresponding SEM images was carried out.

Generally, the quantitative computations were carried out to obtain numerical results, besides the qualitative ones from the SEM images. The quality of the SEM images varied, where some SEM images had less noise and sharper features than others (compare Figure 8 and Figure 9). This issue had highly affected the computations of the SEM images. It was more difficult to identify the nanoparticle boundaries during the thresholding and segmentation in MATLAB whenever the SEM images included lots of noise and reduced sharpness. An inaccurate nanoparticle boundary identification is problematic as it means inaccurate quantification of diameters, roundness metrics, compactions and coverages. To solve this problem, each SEM image was examined separately and given a special threshold value to distinguish the background from the particles, such that the noise effect is as low as possible. However, even after this effort, the returned numerical results were examined, and it was found that noise was occasionally detected as particles and given diameter values between 1 and 7 nm. To solve this problem, an extra computation step through which all image features that were identified as particles with numerical diameters smaller than 7 nm were removed before constructing the numerical distributions that are presented in Figures 8-13. Otherwise, the consequence of not eliminating such noise would have been, amongst others, smaller invalid mean particle diameters.

One speculation, in this case, was whether by excluding data points with diameters smaller than or equal to 7 nm, actual nanoparticles were excluded from the calculations. However, based on the studied data, this is very unlikely because a population of the images was visually examined at a zoomed mode, which revealed that any identified image features with diameters up to 7 nm had no normal particle-like features.

For all the MATLAB calculations of the diameters, roundness metrics, coverage and compaction values, only one sample region, characterized at a 200,000x magnification, was used for each experiment. Investigating more images and/or larger regions could have led to changes in the obtained mean values. However, during the characterizations, images with lower magnifications (80,000x in Appendix II) were investigated to ensure that the characterized sample regions at 200,000x magnification show similar trends, in terms of particle distribution and sizes, as other sample regions. That is, the characterized regions were judged as being good representations of their corresponding samples such that characterizing other regions should give similar mean values for particle diameters, roundness metrics, coverages and compactions.

The accuracy of the results is also highly related to the coverages of the samples, as these reflect the number of data points that are being processed for each experiment as was mentioned earlier in relation to experiment 10. Future experiments with higher, as well as similar, coverages must be carried out and compared to examine the results in a statistically better way.

In summary, variable diameter and roundness metrics were obtained from the experiments where no agglomeration was present. The best mean diameter (smallest) and mean roundness metric (largest) were 19.58 nm respective 0.41, which were yielded in experiment 1.

5.2 Particle Composition

The effect of the electrode types and combination on the elemental composition of the particles was studied using experiments 11 and 12 (Table 2), where NiMo-NiMo respective NiMo-Mo electrode combinations were used. The rest of the system parameters were kept like those employed in experiment 1, from which the best mean particle diameter and highest roundness metric were obtained (Table 5).

Due to constraints regarding the sensitivity of the measurement device to particles, a high particle coverage on the substrate was required. This was ensured by depositing for a longer time than what was done for experiments 1-10 (Table 2). Besides, the particle size setting in DMA2 was changed to 20 nm (instead of 12 nm as in experiment 1), which helped reduce the required deposition period.

Five spectra were obtained from different substrate regions for experiments 11 and 12. The atomic compositions in terms of Ni:Mo were then computed, and these are presented in Figure 15 for experiment 11 and in Figure 16 for experiment 12. The corresponding SEM images and EDXS spectra are presented in Appendix IV.

COMPOSITION USING NiMo ELECTRODES

■ Ni ■ Mo

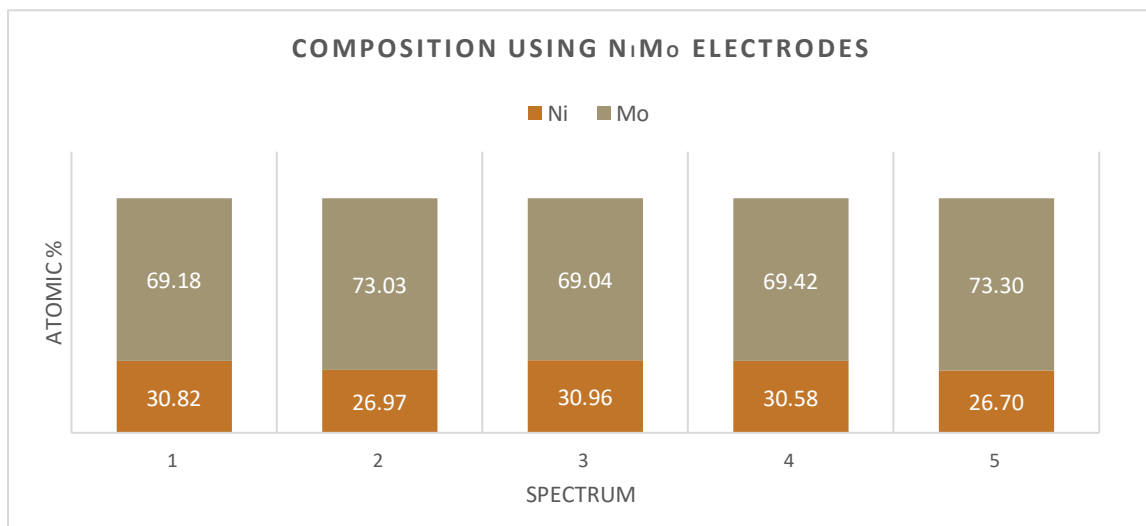| SPECTRUM	Ni	Mo
1	30.82	69.18
2	26.97	73.03
3	30.96	69.04
4	30.58	69.42
5	26.70	73.30

Figure 15. Mean composition from 5 different regions of the sample obtained from experiment 11 using NiMo-NiMo electrodes. The error in the composition approximation is ± 2.00 %.
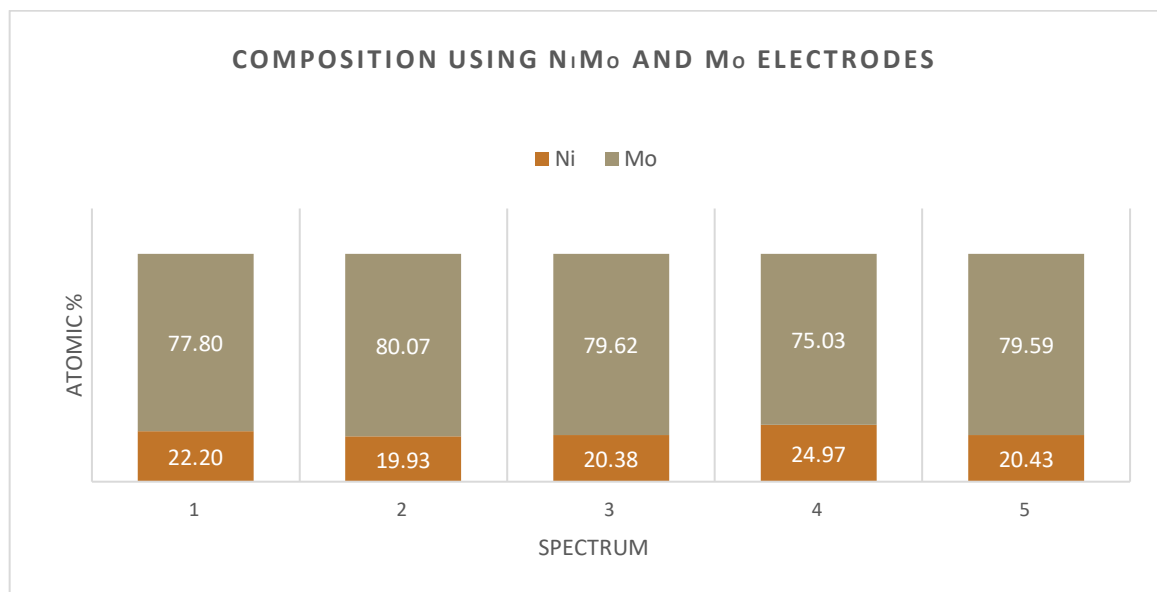
Figure 16. Mean composition from 5 different regions of the sample obtained in experiment 12 using NiMo-Mo. The error in the composition approximation is ± 2.00 %.

Considering Figure 15 and 16, the following results could be deduced.

- The Ni:Mo atomic composition varied between the spectra of experiments 11 and 12. The atomic ratio of Mo that was yielded using NiMo-NiMo was larger than that obtained using NiMo-Mo.
- Using NiMo-NiMo electrodes (experiment 11) gave a mean Ni:Mo atomic composition of 29.21:70.79 ± 2.17; i.e. approximately 3:7 (corresponds to a mass ratio of 20.81:79.19 ± 2.66).
- The mean Ni:Mo composition that was obtained using NiMo-NiMo electrodes was similar to that of the original electrodes.
- Using NiMo-Mo (experiment 12) gave a mean Ni:Mo atomic ratio of 21.58:78.42 ± 2.09); i.e. approximately 2:8 or 1:4 (corresponds to a mass ratio 13.54:86.46 ± 2.88).

The uncertainty of the generated composition values by the EDXS is 2 %, which is considered acceptably high. The compositions that were obtained using NiMo-NiMo or NiMo-Mo electrodes were similar to the original compositions of the electrodes, which is reasonable and agrees with other results in previous studies, where the obtained nanoparticle compositions were similar to those of the electrode materials [3].

An interesting point that was examined is whether the electrode polarity affected the amount of material that was yielded from different electrodes. This speculation is due to previous reports, where more of the anode material was present in the yielded nanoparticles in one study [12], while more of the cathode material in another [13]. To examine this, the results from the composition experiment where NiMo-Mo electrodes were employed, with Mo as the anode, were considered. The obtained wt ratio of Ni:Mo was 13.54:86.46 wt %. The Ni proportion could be assumed to have completely been yielded from the cathode electrode, which was an NiMo electrode, since the

41

anode was made of pure Mo. Assuming that each particle that was yielded from the cathode had the same composition as that of the cathode: 3:7 at or 21:79 wt Ni:Mo, for each 21 g Ni nanoparticles released from the cathode, 79 g Mo nanoparticles must have also been released from the same cathode. Assuming that the yielded total mass of the nanoparticles is 100 g and that the 13.54 wt ratio of Ni were from the cathode: 13.54 g Ni/100 g nanoparticles, then the companying Mo mass must have been 13.54 g * 79/21 = 51 g. This gives a total of 65 g (Ni and Mo mass) from the cathode; i.e. cathode material, with the remaining 35 g supposedly being the anode material. This does show that more of the cathode material (65 wt %) is present among the yielded nanoparticles in this study. However, no experiments with Mo in the cathode side were carried out, meaning that it remains uncertain whether a similar trend would have been deduced if the electrode polarities were switched.

Obtaining more of the cathode material, in this case, could be related to the different physical properties of the material of the electrodes, including boiling points and the enthalpies of evaporation. More electrode material is lost if the material has a low evaporation enthalpy based on the reviewed literature [3] (and low boiling points). When considering the evaporation points and evaporation enthalpies of Ni and Mo, Mo has larger ones, meaning that it was physically harder for Mo to evaporate from its electrode, which was the anode. In the other NiMo cathode electrode, the alloying of Mo with Ni must have decreased the overall material enthalpy to one between the enthalpies of Ni and Mo, making it easier for NiMo to evaporate from its electrode. Thus, less anode material and more cathode material evaporated and were yielded in the nanoparticles. This discussion could also be supported by recalling the reported high Ni composed nanoparticles that were generated through a SDG system, using pure Ni and pure Mo electrodes study [2]. The atomic compositions were 66:34 and 72:28 Ni:Mo at %, revealing that Mo electrode evaporation was apparently much lower than that of the Ni electrode.

For the compositional analysis, a highly nanoparticle-covered substrate was required as the used EDXS equipment was insensitive to low coverages. For this reason, the deposition was carried out for a long period of time in experiments 11 and 12, giving a particle-count-based coverage of about 50 % in both samples. Besides the setting of DMA2 was changed so as to release particles as large as 20 nm (instead of 12 nm as in the rest of the experiments). This was done to allow yielding more particles within a reasonable experiment duration, ensuring a sufficiently high coverage for the EDXS measurements. However, studying the SEM images that correspond to experiments 11 and 12 (see Appendix IV), it was noted that a high level of agglomeration was yielded. This was unexpected as all the operation parameters that were employed for these experiments, except for the DMA settings, coverage time and electrodes, were kept similar to those in experiment 1, from which nanoparticles with good morphological properties were yielded. Agglomeration was thereby unexpected, and the main reason to why it was obtained in these experiments is unclear. However, it is possible that the higher coverage and/or allowing larger particles through the DMAs had enhanced agglomeration to occur. To demonstrate this, more experiments to investigate the effect of different coverage levels, as well as the effect of setting DMA2 to allow through particles with sizes larger than 12 nm, must be carried out.

One uncertainty factor due to carrying out the compositional analysis on agglomerated nanoparticles was however whether the detected agglomerates were representative of the particles that were yielded in the other experiments (like experiment 1), and whether the agglomerates are mostly NiMo, Ni or Mo primary particles. The difference is that the latter two types are undesired as these do not enhance catalysis as the NiMo particles would do. All types of particles being present in the detected nanoparticles bulk is a very likely scenario, but the best one would be having mostly NiMo primary particles with the detected compositions. In such a case, the detected compositions are definitely corresponding to the mean ones of primary NiMo particles. Understanding this requires particle sensitive characterization techniques, like Transmission Electron Microscopy, to be used in the future analysis for a more detailed primary particle compositional analysis, even without the requirement of high sample coverage.

However, the incident of yielding a high level of agglomeration upon carrying out a longer deposition in experiment 11 and 12, regardless of employing system parameters that were found to enhance sphericity and low agglomeration, reveals that the coverage was likely one detriment factor for the agglomeration of the nanoparticles. This might have been due to electromagnetic attractions between the deposited particles and particles entering the deposition chamber, probably allowing a more energetically favored material distribution. It is also possible that particles underwent surface diffusion after being deposited, ending up forming agglomerates. However, this latter is not very likely as the SiOx surface lacked line defects that would act as channels for the nanoparticles to diffuse through. The smoothness of the surface of the SiOx support could be seen in all the presented SEM images presented in Figure 5.

SiOx wafers were used as the substrate or support for the nano-catalysts, but as a normal practice, hydrotreating catalysts are supported on alumina. Using SiOx instead of alumina was suspected of having resulted in different catalyst properties from the real-life ones. However, using SiOx for these nano-catalysts was intended to facilitate an evenly distributed nano-catalysts deposition on the support surface, not bulk sites, since the deposition of nano-catalysts within internal sites would have complicated the particle characterizations. Being able to clearly identify and characterize the nano-catalysts on the surface was very advantageous and one main motive of this work. It allowed identifying the properties of the catalytic phase, regardless of its interference with the interior support structure. However, it is very intuitive that the support properties highly affect the overall catalyst behavior and in order to deduce whether there is a significant difference in the catalysts behavior upon using the different supports, characterizations of catalysts with alumina as the support must be compared to ones with SiOx.

To sum up, nanoparticles with approximately 1:4 and 3:7 mean Ni:Mo atomic compositions were yielded using NiMo-Mo respective NiMo-NiMo electrodes.

5.3 Additional Characterizations: The Reducibility of Model NiMo Nano-catalyst

XAS measurements were carried out on the additional nano-catalyst samples and reference industrial catalysts, generating XANES to compare their reducibility. The XANES spectra were plotted[1] and are presented in Figure 17-20.
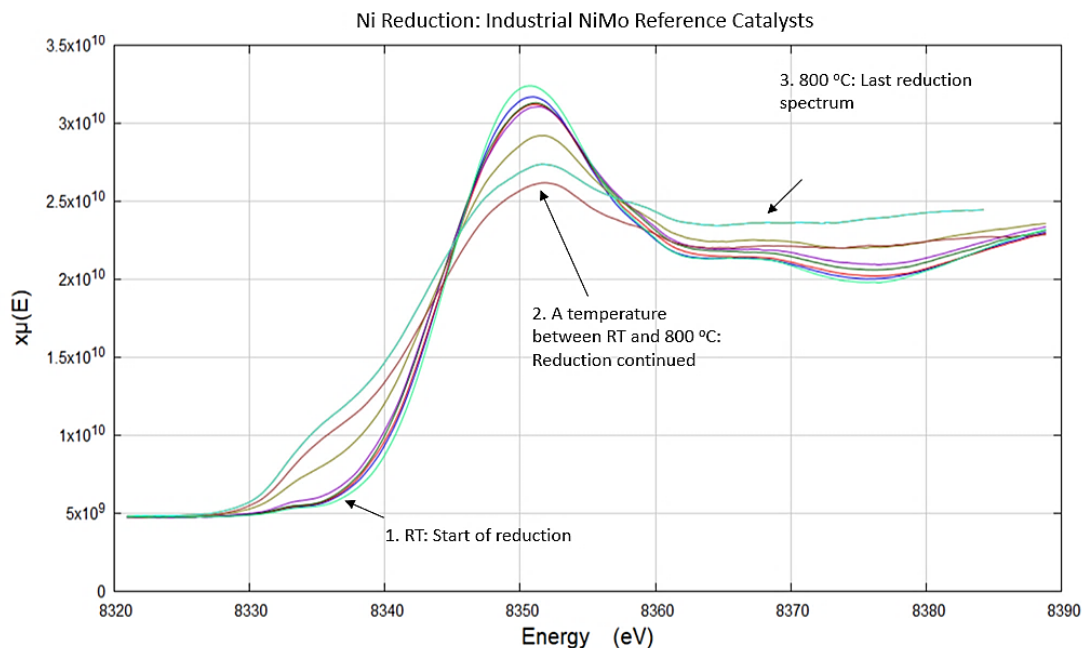

Figure 17. Ni XANES from the industrial catalyst sample. The spectra were obtained during reduction and temperature ramping between RT and 800 °C.
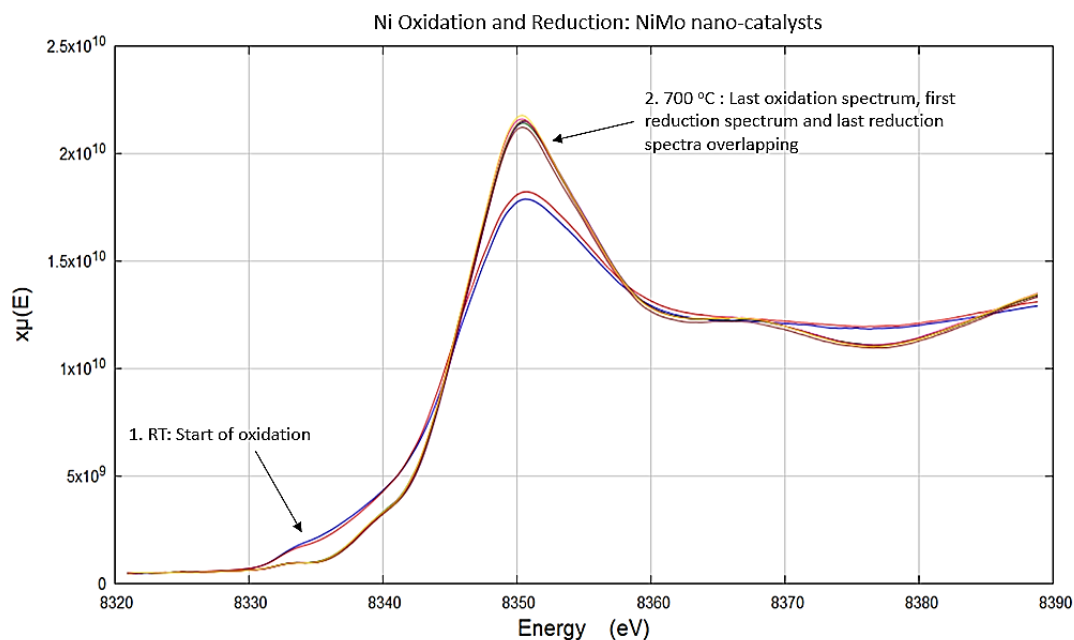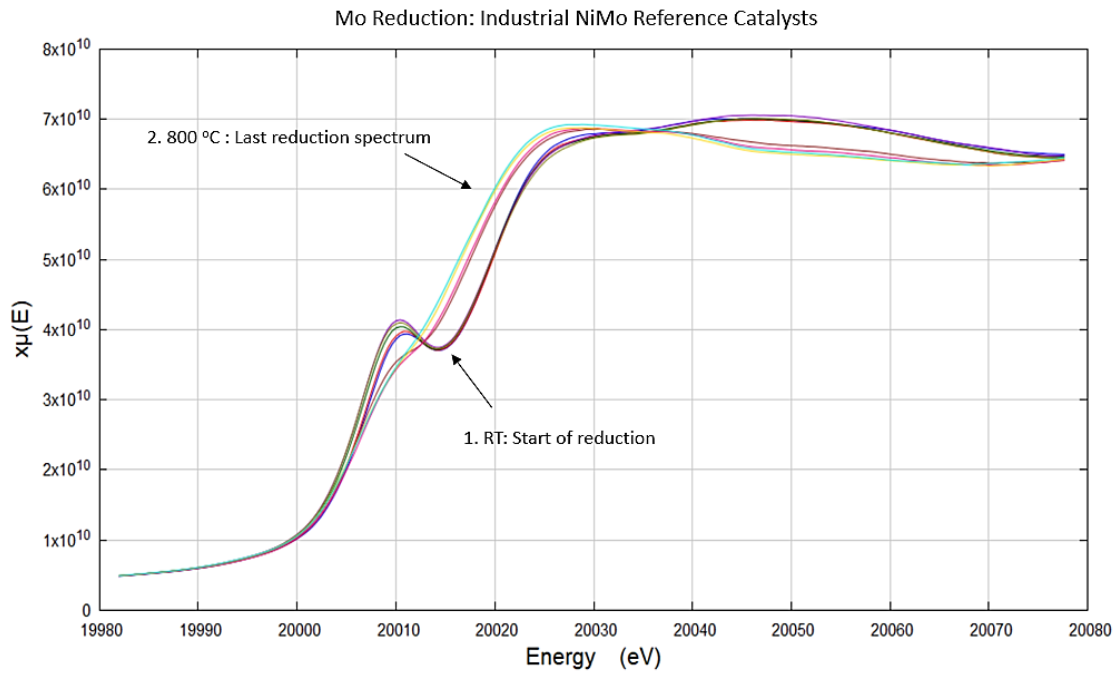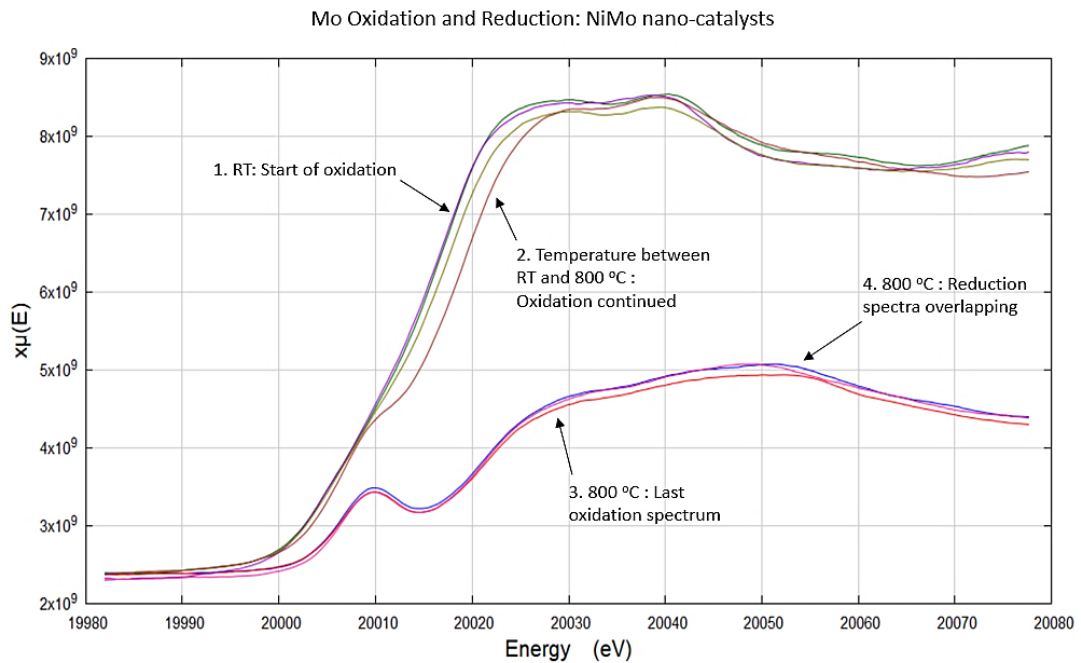

Figure 18. Ni XANES from the nano-catalysts. The spectra were obtained by oxidizing during ramping between RT and 700 °C, then reducing at 700 °C.

---

[1] The spectra were plotted using the software Demeter, Athena, which was obtained from https://bruceravel.github.io/demeter/.

Figure 19. Mo XANES from the industrial catalyst samples. The spectra were obtained during reduction and temperature ramping between RT and 800 °C.

Figure 20. Mo XANES from the nano-catalysts. The spectra were obtained by oxidizing and temperature ramping between RT and 800 °C, then reducing at 800 °C.

From the Ni and Mo XANES shown in Figure 17-20, the following was pinpointed.

o   Ni in the industrial catalysts was reduced during ramping from RT to 800 °C, where at the highest temperature, the pre-edge shifted to higher energy and the peak decreased.

45

- o For the Ni XANES from the nano-catalyst sample, the edge position shifted to lower energy value at the end of the oxidation process at 700 °C, which was probably due to an increase in the oxidation state.

- o At 700 °C and after shifting to the reductive gas, the Ni in the nano-catalyst sample did not show any reduction, which is evident by the overlapping of the last oxidation spectrum at the end of the temperature ramping, the first reduction spectrum at 700 °C and the last reduction spectrum, also at 700 °C (point 2 in Figure 18). That no reduction took place was also detected by comparing the reference industrial catalyst and the nano-catalyst Ni spectra, where the shift (1-3) that was detected in Figure 17 was absent in Figure 18 after the start of the reduction.

- o Similarly, comparing Figure 19 and 20, Mo in the industrial sample became more reduced during the temperature ramp from RT to 800 °C. In Figure 20, oxidation of Mo in the nano-catalyst occurred significantly as the temperature was ramped between RT and 800 °C, but no reduction occurred when the gases were shifted at 800 °C, giving the almost overlapping spectra at 800 °C (points 3 and 4 in Figure 20).

- o The two Mo XANES from the industrial and nano-catalyst samples were not very similar, where all the spectra in the first intersect at some point after the edge, but not in the latter. However, the general shapes of the curves among the two were similar.

Reducibility is one important factor that influences the applicability of such model catalysts, which is essential as catalyst sulfidation, which involves its reduction, must always be carried out before the catalyst can catalyze hydrotreating reactions, as was explained earlier. The XAS spectra for the industrial samples were obtained to facilitate the comparison between these and the generated model ones. However, while no oxidation was carried on the industrial catalysts, the nano-catalyst samples were firstly oxidized to ensure that they are, just like in the usual process of catalyst activation, fully oxidized prior to reduction (sulfidation).

Neither Ni nor Mo in the model nano-catalysts underwent any isothermal reduction at 700 and 800 °C, even though the reference industrial ones were successfully reduced. As an attempt to explain why reduction did not occur, other studies where Mo and Ni reduction was investigated were reviewed. It was reported in one that the induction period (a period during which a reaction rate is slow) of an isothermal Mo reduction at 400 °C was two hours [17]. For Ni, the reduction was previously carried out at 350 °C, and it was reported that the level of reduction increased with time [18].

Considering the current reduction procedure, the temperature that was employed during the isothermal reduction was twice as much as those used in the latter two studies. Also, the reaction period of the current isothermal Ni and Mo reductions was about one hour. As a rule of thumb, the rate of reaction increases with temperature, meaning that the rates of reactions of Ni and Mo should have been higher than those at 350 and 400 °C. Followingly, a significant level of reduction should have been detected after one hour. However, this was not detected, meaning that the rule of thumb that increasing the temperature increases the rate of reaction was inapplicable in this case.

The reduction is generally an exothermic process. Employing 800 °C might have been thermodynamically unfavorable, especially as Ni and Mo were previously reduced at 350 respective 400 °C, and this could have been the reason to why reduction did not occur.

The reduction of the nano-catalyst was not completed in the same way as for the reference industrial catalysts, where the firstly named were reduced isothermally and the latter was reduced under a temperature ramping program. Employing a ramping program for the nano-catalysts could have enhanced their reduction to take place.

A possible reason was also that at the high temperature that was employed during the isothermal reduction, the phase and structure of the nano-catalysts might have changed in such a way that prohibited reduction, especially that reducibility was suggested to be sensitive to the structure of the material [17]. The nanoparticles might have diffused into the support material giving structural changes. This is highly possible since the diffusivity of nanoparticles is generally high, as explained earlier, and increasing the temperature enhances diffusivity.

Another factor that could have influenced reduction to not occur is heat transport limitations resulting from the measurement chamber layout. The heater that heated up the chamber was not placed in direct contact with the sample, where there was an empty gap between the two. The temperature of the sample surface might have, therefore, never reached the desired 700/800 °C due to the insulating gap, which was gas-filled. Also, the gases (oxidative and reductive) were supplied from their sources at room temperature, and it was assumed that these would get heated within the measurement cell. Gases are known to have low heat transport coefficients, which means that the assumption that the flowing gases were sufficiently heated was likely untrue and that even the gases temperature had probably never reached the desired 700/800 °C.

The pressure of the reductive gas (5 % H_2 in N_2) was atmospheric pressure. Increasing the pressure could have enhanced the reduction of the nano-catalysts to occur.

Regarding phase identifications from the XANES, none were carried out in this work as it was unnecessary as no reduction shifts were obtained. However, identifying the present phases could have led to a more detailed understanding of the oxidation and reduction processes of the model nano-catalysts.

In summary, the generated nano-catalysts were successfully oxidized during a temperature ramping from RT to 700 and 800 °C and oxidative gas at normal pressure, but they did not show any isothermal reduction after their oxidation at 700 and 800 °C and reductive gas at normal pressure. The reduction is involved in catalyst sulfidation for activation. Observing reducibility properties that are comparable to those of the industrial catalyst is a signal that the generated model catalysts

are suitable for use as representatives of industrial catalysts in model systems during catalyst development. Thus, further studies with the aim of finding suitable reduction conditions for these nano-catalysts are required. Higher gas pressures and lower isothermal reduction temperatures can be tried, with perhaps longer reaction periods.

5.4 Assessment of the Experimental Design

In this work, experiments were carried out to generate NiMo nano-catalysts with specific morphological and compositional criteria. For this purpose, 12 experiments (aside from the additional ones for generating nano-catalysts for the extra XAS characterizations) were carried out and investigated pairwise to understand the effect of the six chosen system independent parameters. Each of these was tested at two different levels. Doing this, nano-catalysts with good sphericity, sizes below 25 nm and the desired composition could successfully be generated, showing that the experimental design was sufficient for reaching the pre-set research goal. The experiments, however, lack replicates. This limits the trustworthiness of the findings and makes it impossible to assess the reproducibility of the system. However, this was compensated for by doing t-tests and outlier tests (Chapter 5.1.2), as well as by comparing the current findings to previously reported ones whenever suitable.

Correlations like that between the spark frequency and the discharge voltage, which was found to affect the mean particle size distributions, as explained by equation 3, were not fully examined. This is because the experiments through which the effect of different discharge voltage levels was investigated generated agglomerated particles. Therefore, these results were not assessed for mean particle diameters, roundness metrics, etc. More experiments, where the discharge voltage levels are combined with other system parameters than the employed ones, can possibly result in the generation of nanoparticles with better characteristics. Besides, some of the unvaried system parameters, such as the gas type, were also previously reported to have a significant effect on the characteristics of spark discharge generated nanoparticles. As these were kept constant, their effect in combination with other parameters could not be assessed, and future experiments where these parameters are studied must be carried out.

The used carrier gas was pure nitrogen. Hydrogen gas could have been used in combination with nitrogen gas to minimize the risk of nanoparticle oxygen contamination. This was not done in this work as a cost-saving effort. Besides, the system could be vacuumed before each experiment and ensured to not exhibit any air leakage.

The employed system had practical limitations, which imposed limitations on the settings of the experiments. One important limitation was that the DMAs, as well as the particle counter, were calibrated for 1.68 L/min carrier gas flowrate. As explained earlier, this forbade employing other flowrates, such as the tested 4.00 L/min, through the system except for the SDG chamber. Another system limitation was that the DMAs could not be set to allow particles smaller than 10 nm through, which limited the possible settings. Being able to employ 4.00 L/min through the DMAs

and particle counter and/or being able to set the DMAs to release particles with sizes below 10 nm might have resulted in nanoparticles with different characteristics compared to the present ones.

Regarding the experimental system stability, the parameter readings were always monitored during the experiments and deviations in some of these, including discharge current, depositing voltage and particle count was detected. One example was setting the discharge current at 15 μA but getting a reading of 8 μA. Another was continuous oscillations in the discharge voltage. The discharge voltage readings also showed a gradual increase during operation, besides the normal reading oscillation. This gradual increase was probably occurring due to the electrode material being consumed during operation and the inter-electrode gap increasing consequently. This was compensated for by manually adjusting the gap, as was described earlier.

The detected reading deviations were expected to have influenced the nanoparticle generation. To conclude whether the effect of these deviations was significant or not, readings from 5 spontaneously chosen experiments, 3 meant to be at 2.5 kV and 2 at 1.4 kV, were registered and the means, as well as the mean square errors (MSE), were calculated. For the 2.5 kV readings, a mean of 2.5 kV was obtained, with a mean MSE of 0.002, and for the 1.4 kV experiments, 1.4 kV was the mean with 0.0007 as the MSE. This showed that there was no pronounced effect due to the oscillations or gradual gap increase. That is, the discharge voltage oscillations were stable, and the manual control of the inter-electrode gap to maintain the desired discharge voltage was successful.

Another reading oscillation that is believed to have affected, amongst other things, the particle count-based coverage calculations was the particle count. It was noted that the particle count varied from one experiment to the other, even when similar operation parameters were employed among the experiments. Besides, the particle count reading increased throughout the operation period during each experiment. Such an increase in the particle count could be due to an increase in the level of evaporation from the electrodes as they were getting used up during operation. To explain this link, Llewellyn Jones model [15] was considered, which explains that when less material volume/surrounding is present, less heat can be dissipated via conduction. Followingly, heat dissipation can mostly occur via electrode evaporation. Similarly, the volume of the electrodes must have gradually decreased as they were getting used up during sparking, enhancing more evaporation from the electrodes to take place, resulting in the observed increase in the particle count towards the end of each experiment.

In summary, the adopted experimental design facilitated understanding the effect of many system parameters and allowed yielding nanoparticles with morphological and compositional specifications that are within the desired ranges. However, further investigations, where more parameters are considered, can lead to the generation of nanoparticles with better characteristics.

Chapter 6: Conclusion

The generation of NiMo nanoparticles, via the spark discharge technique, for application as model hydrotreating catalysts, was investigated. Combinations of different levels of various operation parameters, namely the electrode type, discharge voltage, gas flowrate through the SDG chamber, furnace temperature, depositing voltage and number of DMAs that are employed in the system, were investigated. It was concluded that nanoparticles with various morphological and compositional specifications were consequently generated. Among these, nanoparticles with specific characteristics, including:

- o no agglomeration,
- o high sphericity as indicated by the mean roundness metric value 0.41,
- o a mean particle diameter of 19.58 nm,
- o a composition 1:4 atomic Ni:Mo,
- o and high particle compaction of 99.7 %.

that make them suitable for use as model hydrotreating catalysts, were yielded. These characteristics were obtained when the following system parameter levels were employed:

- o NiMo-Mo electrode combination, with Mo as the anode,
- o 2.5 kV discharge voltage,
- o N_2 carrier gas, with a flowrate of 1.68 L/min through the SDG chamber (as well as the rest of the system),
- o 1200 °C furnace temperature,
- o 7 kV depositing voltage,
- o 1 DMA.

Employing NiMo-NiMo as the electrodes, 4 kV as the depositing voltage and 2 DMAs also gave non-agglomerated, spherical nanoparticles, but with different mean compositions, larger mean particle diameters and lower roundness metrics.

Employing NiMo-Mo electrodes, an atomic composition of about 1:4 Ni:Mo was obtained, while employing NiMo-NiMo, a composition of about 3:7 Ni:Mo was gotten, leading to the conclusion that the average composition of the nanoparticles that were generated using bimetallic electrodes was similar to that of the electrodes.

Agglomerated nanoparticles were obtained in all experiments when 1000 °C was employed as the furnace temperature. On the contrary, agglomeration was eliminated in all experiments when 1200 °C was instead applied, leading to the conclusion that increasing the furnace temperature significantly enhances the elimination of particle agglomeration and improves sphericity. Agglomeration was also obtained in all experiments when 1.4 kV discharge voltage and 4.00 L/min gas flowrate through the SDG chamber were employed. High coverages were also correlated with

obtaining agglomerated particles as agglomeration was present in all the experiments that had high coverages.

Some morphological and compositional trends that were reported in the reviewed literature were also confirmed by the current findings. These include correlating the use of electrode components with lower ionization potentials and evaporation enthalpies to yielding particle with reduced sizes. Increasing the furnace temperature was concluded to enhance sphericity and non-agglomeration, as was concluded in other studies. A reduction in the branching level of agglomerates upon yielding a higher amount of magnetic Ni among the generated nanoparticles (due to increasing the discharge voltage, which supposedly gave increased spark energy and a higher evaporation level) was also confirmed. Finally, it was also concluded, in agreement with some previously reported results, that more of the cathode material was yielded in the samples.

Other trends that were not necessarily reviewed in literature but discovered in this work included the correlation between the particle compaction and roundness metric, where high particle compaction values and high roundness metrics were simultaneously obtained in several samples.

Generally, the Spark discharge technique could be used for generating nanoparticles with morphological and compositional specifications that make them suitable for use as model hydrotreating catalysts, mirroring the potential of this technique in the generation of model catalysts. The generated model nano-catalysts showed however inadequate reducibility, as was revealed by the XAS characterizations. Significant oxidation of both Ni and Mo occurred, but neither Ni nor Mo were reduced at 700/800 °C after about one hour. This is challenging as the inadequate nano-catalysts reducibility limits their suitability for application in model systems to represent industrial hydrotreating catalysts. Several factors were discussed as possible reasons to the observed nano-catalyst irreducibility, including an unsuitable choice of reduction temperature, gas pressure, reaction time and/or XAS system layout.

As future efforts, the reducibility of these NiMo model nano-catalysts must be addressed, where different reduction temperatures and system parameters are more closely considered. This will provide a good assessing criterion of the potential of spark discharge generated nanoparticles as model catalysts. The characterization of such nano-catalysts, during and after exposure to actual chemical systems, must also be carried out.

Besides, the samples that were used for the compositional characterizations were generated with very high coverages, as was discussed, and this probably enhanced the observed agglomeration. Even though reasonable findings were concluded in terms of a match between the average electrode compositions and the average nanoparticle compositions, the primary particle nature and its composition remain uncertainly defined. Thus, samples with non-agglomerated spherical particles, similar to the ones in the other experiments, must be generated and characterized via

particle sensitive techniques, such as TEM, to enable conclusions in terms of the compositions of individual nanoparticles.

Regarding the adopted experimental system, future investigations of more system parameters, such as gas type, can help generate nanoparticles with better characteristics. Furthermore, developing the spark discharge generation technique can be considered. Such development work can, for example, target the system design to examine the possibility of generating commercial catalysts. This will be advantageous as this technique provides a purer catalyst synthesis route and is more environmentally friendly.

References

[1] C. Hulteberg et al., "A new method for structured catalyst development", Department of Chemical Engineering, Lund University. Mar. 2019.

[2] S. Blomberg et al., "Bimetallic Nanoparticles as a Model System for an Industrial NiMo Catalyst". *Materials,* vol. 12, pp. 1-13, Nov. 2019.

[3] N. Tabrizi et al., "Generation of nanoparticles by spark discharge," *Journal od Nanoparticle Research*, vol. 11, pp. 315-322, Feb. 2009.

[4] S. Navalon et al., "Nanoparticles as Catalysts," *Nanomaterials (Basel).* Vol. 6, Jun. 2016. [Online]. Available: https://www.ncbi.nlm.nih.gov/pmc/articles/PMC5224611/. [Accessed Feb. 9, 2020].

[5] R. Dante, *Handbook of Friction Materials and Their Applications,* ScienceDirect, 2016. [E-book] Available: https://www.sciencedirect.com/topics/chemistry/bulk-melting-temperature.

[6] A. Lizunova et al., "Influence of the sintering temperature on morphology and particle size of silver synthesized by spark discharge," *IOP Conference Series: Materials Science and Engineering*, vol. 307, 2018.

[7] G. Ertl et al., *Handbook of Heterogeneous Catalysis.* Wiley, 1997, pp. 2696-2700, 2707, 2709-2710.

[8] H. Rase et al., *Handbook of Commercial Catalysts, Heterogeneous Catalysts.* CRC Press, 2000, pp. 317-322, 330-331, 332.

[9] Y. Xu et al., "Upgrading of liquid Fuel from the vacuum pyrolysis of biomass over the Mo-Ni/γAl_2O_3 catalysts," *ELSEVIER*, vol. 33, pp. 1030-1036, May. 2009.

[10] N. Chen et al., "Effect of reduction temperature of $NiMoO_{3-x}$/SAPO-11 on its catalytic activity in hydrodeoxygenation of methyl laurate," *ELSEVIER*, vol. 174-175, Sep. 2015. [Online]. Available: https://www.sciencedirect.com/science/article/abs/pii/S0926337315001320. [Accessed Feb. 6, 2020].

[11] B. Meuller et al., "Review of Spark Discharge Generators for Production of Nanoparticle Aerosols," *Aerosol Science and Technology*, vol. 46, pp. 1256-1270, Aug. 2012.

[12] J. Byeon et al., "Spark generation of monometallic and bimetallic aerosol nanoparticles," *Journal of Aerosol Science*, vol. 39, pp. 888-896, May. 2008.

[13] N. Tabrizi et al., "Generation of mixed metallic nanoparticles from immiscible metals by spark discharge," *Journal od Nanoparticle Research*, vol. 12, pp. 247-259, Feb. 2009.

[14] M. Boeije et al., "Nanoparticle Production by Spark Ablation: Principle, Configuration, and Basic Steps towards Application," in Spark Ablation Building Blocks for Nanotechnology," Jenny Stanford Publishing, 2020, pp. 55, 74-75.

[15] A. Muntean et al., "Generation of Mixed Nanoparticles by Spark Ablation of Alloys and Spark Mixing," in Spark Ablation Building Blocks for Nanotechnology," Jenny Stanford Publishing, 2020, pp. 171.

[16] S. Ekeroth et al., "Impact of nanoparticle magnetization on the 3D formation of dual-phase Ni/NiO nanoparticle-based nanotrusses," *Journal of Nanoparticle Research*, vol. 21, no. 228, Nov. 2019. [Online]. Available: https://link.springer.com/article/10.1007/s11051-019-4661-8. [Accessed Apr. 30, 2020].

[17] T. Ressler et al., "Time-Resolved XAS Investigation of the Reduction/Oxidation of MoO_{3-x}," *Journal of Catalysis*, vol. 191, p. 75-85, Apr. 2000. [Online]. Available: https://www.sciencedirect.com/science/article/pii/S0021951799927720. [Accessed Apr. 28, 2020].

[18] S. Loiha et al., "Reducibility of Ni and NiPt supported on zeolite beta investigated by XANES," *Journal of Taiwan Institute of Chemical Engineers*, vol. 42, p. 527-532, May 2011. [Online]. Available: https://www.sciencedirect.com/science/article/abs/pii/S1876107010001847. [Accessed Apr. 28, 2020].

[19] National Center for Biotechnology Information, "Nickel," *National Center for Biotechnology Information*, [Online]. Available: https://pubchem.ncbi.nlm.nih.gov/element/Nickel. [Accessed Mar. 9, 2020].

[20] Royal Society of Chemistry, "Nickel," *Royal Society of Chemistry,* [Online]. Available: https://www.rsc.org/periodic-table/element/28/nickel. [Accessed Mar. 9, 2020].

[21] National Center for Biotechnology Information, "Molybdenum," *National Center for Biotechnology Information*, [Online]. Available: https://pubchem.ncbi.nlm.nih.gov/compound/molybdenum#section=Heat-of-Vaporization. [Accessed Mar. 9, 2020].

[22] Royal Society of Chemistry, "Molybdenum," *Royal Society of Chemistry,* [Online]. Available: https://www.rsc.org/periodic-table/element/42/molybdenum. [Accessed Mar. 9, 2020].

Appendices

_____

Appendix I. Hydrotreating Reactions

Typical schematic reactions that occur during hydrotreating are presented below. [8]

Hydrodesulfurization (HDS)

R-SH + H$_2$ ⟶ RH + H$_2$S *(Mercaptans)*

R-SS-R′ + xH$_2$ ⟶ RH + R′H + ½(x-2) H$_2$S *(Disulfides including aromatics)*

Hydrodenitogenation (HDN)

R-NH$_2$ + H$_2$ ⟶ RH + NH$_3$ *(Amines)*

R-NH + xH$_2$ ⟶ R + NH$_3$ *(Pyrrole (R is butane), Carbazole, Quinoline (R is a cyclic hydrocarbon with side chain))*

R-N + xH$_2$ ⟶ R + NH$_3$ *(Pyridine (R is a saturated hydrocarbon))*

Hydrodeoxygenation (HDO)

R-COOH + xH$_2$ ⟶ R-CH$_3$ + ½(x-3) H$_2$O *(Acids)*

R-OH + xH$_2$ ⟶ R + H$_2$O *(Phenols)*

R-O + xH$_2$ ⟶ R′ + H$_2$O *(Furans. R′ is a saturated hydrocarbon)*
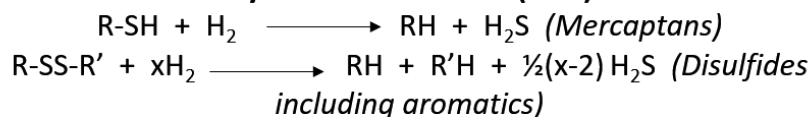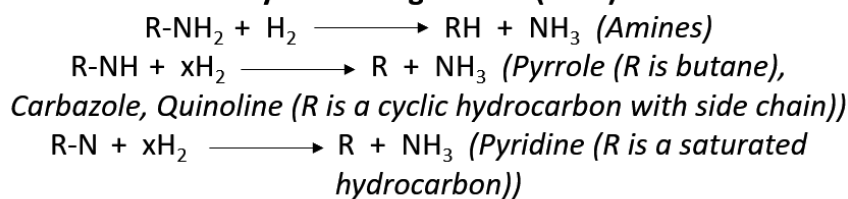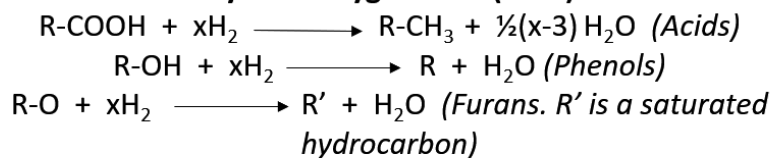
The physiochemical data for Ni and Mo are listed in Table I.1.

Table I.1. Ni and Mo elemental data. [19, 20, 21, 22]

Property	Ni	Mo
Melting Point	1455 °C	2622 °C
Boiling point	2913 °C	4639 °C
Evaporation enthalpy	*Not found in literature*	684 kJ/mol (1st)
Ionization Energy	737 kJ/mol (1st)	491 kJ/mol (1st)

Appendix II. SEM Images at 80 000x Magnification

SEM images at a magnification of 80,000x were obtained for experiments 1-10. These are in presented in Figure A1 below.
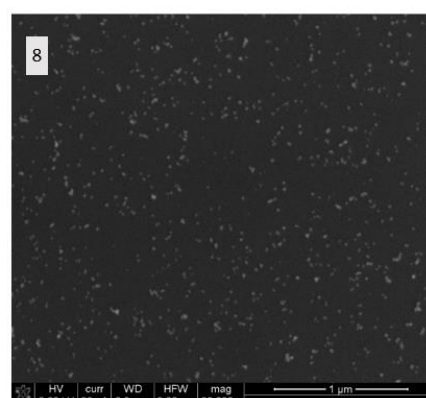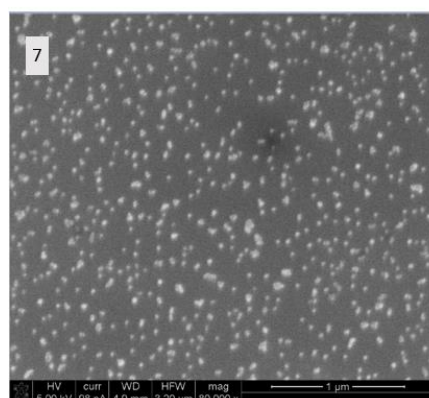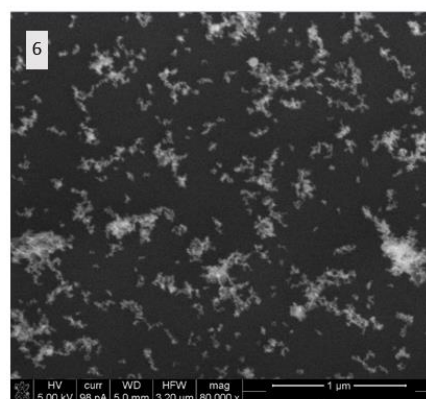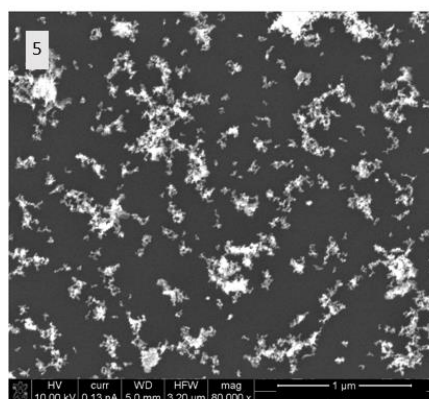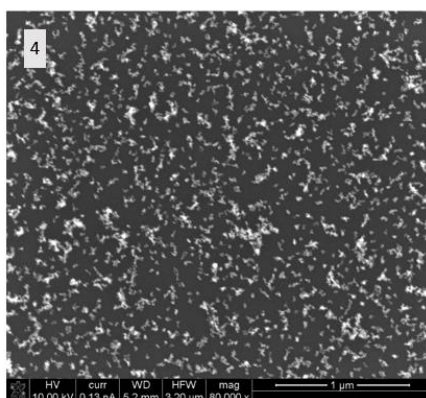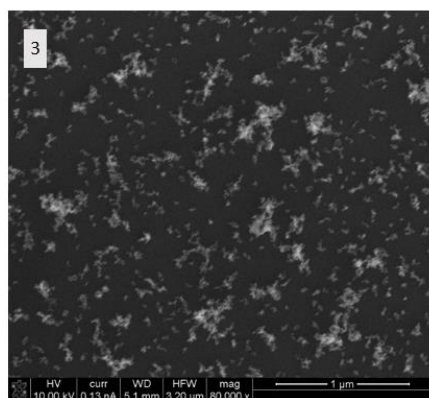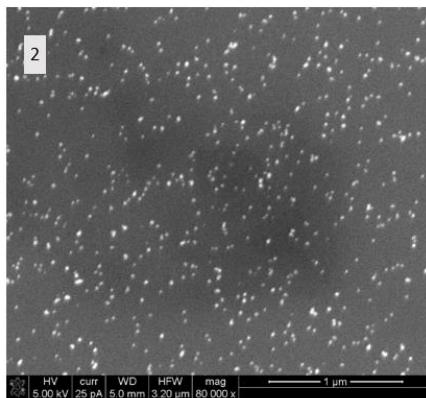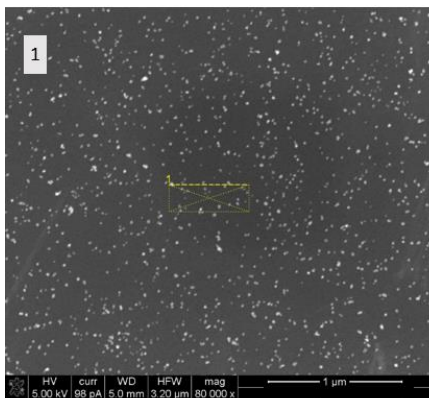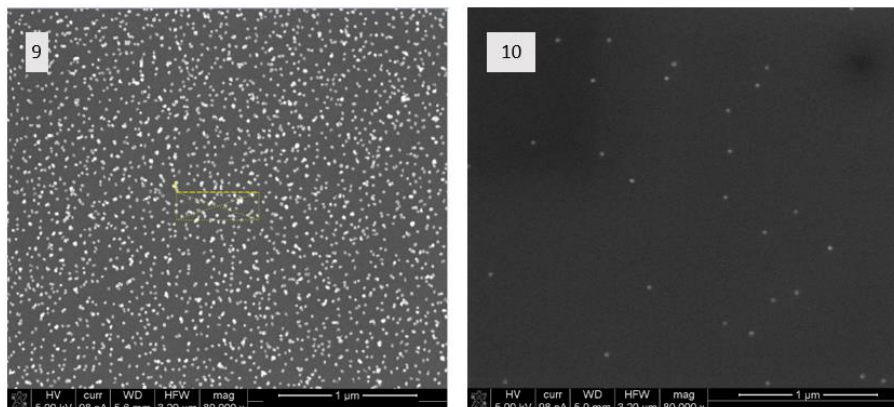
Figure A1. SEM images at 80,000x magnification for experiments 1-10.

Appendix III. Diameter Distribution Curves

The diameters distributions for experiments 1, 2, 7, 8, 9 and 10 were plotted together to clarify their relative differences. These are presented Figure A2 below.
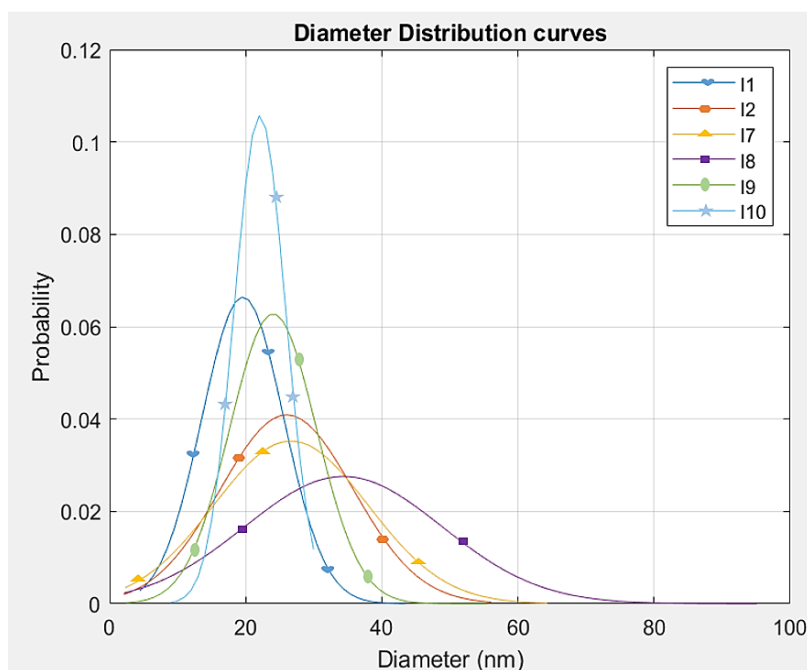
Figure A2. The diameter distributions for experiments 1, 2, 7, 8, 9 and 10.

Appendix IV: EDXS Spectra and the Corresponding Electron Images

The EDXS spectra, that were obtained from different regions of the samples from experiments 11 and 12, for the compositional analysis of the nano-catalysts are presented below.
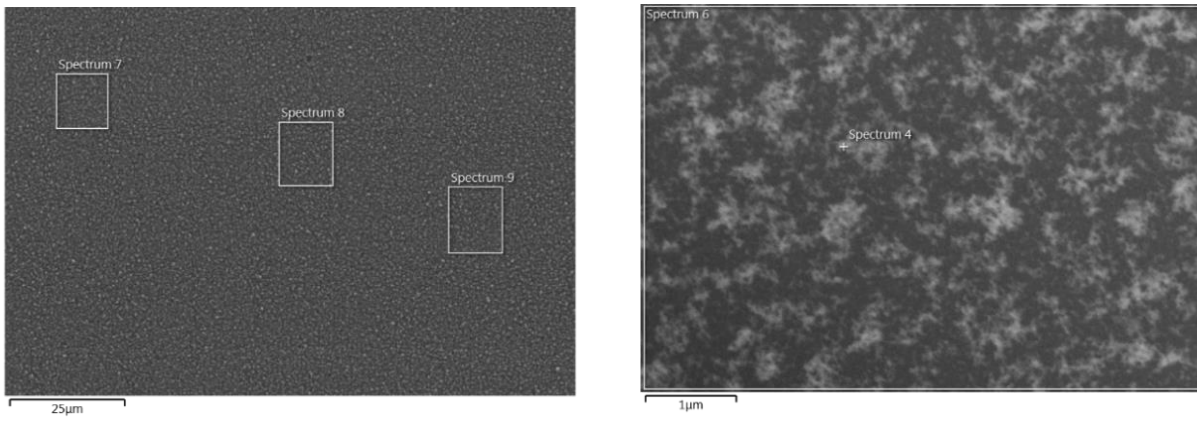
Experiment 11
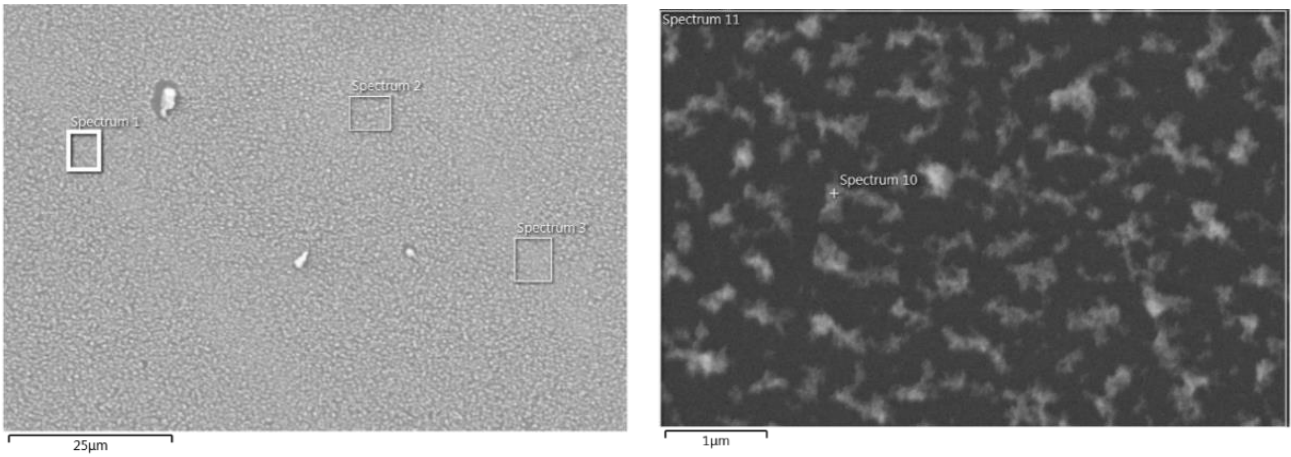
Figure A3. SEM images from experiment 11 with the selected regions for the EDXS characterization marked.
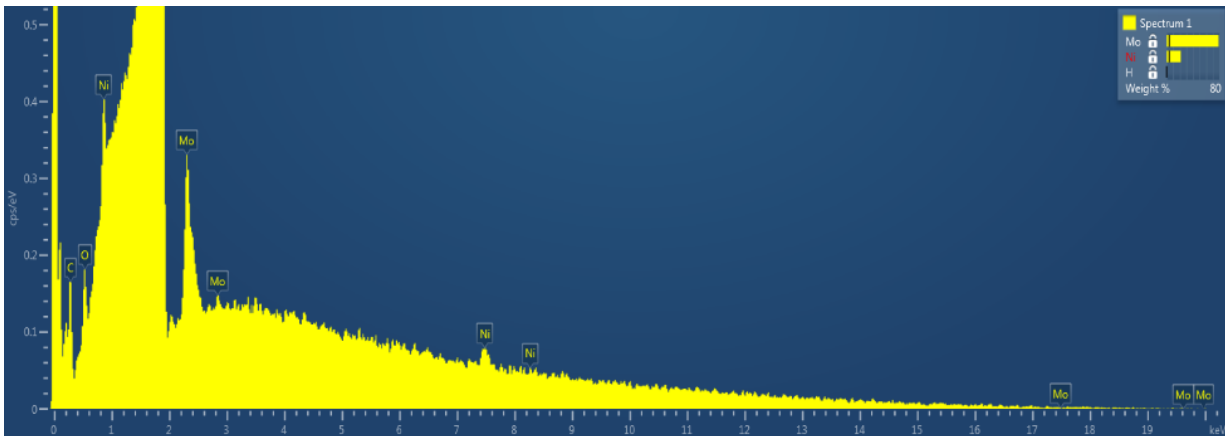
Spectrum 1
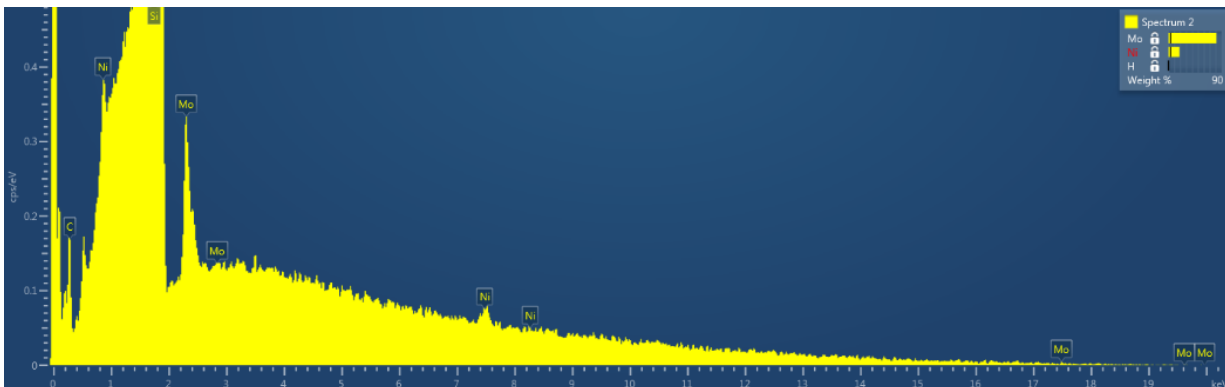
Spectrum 2
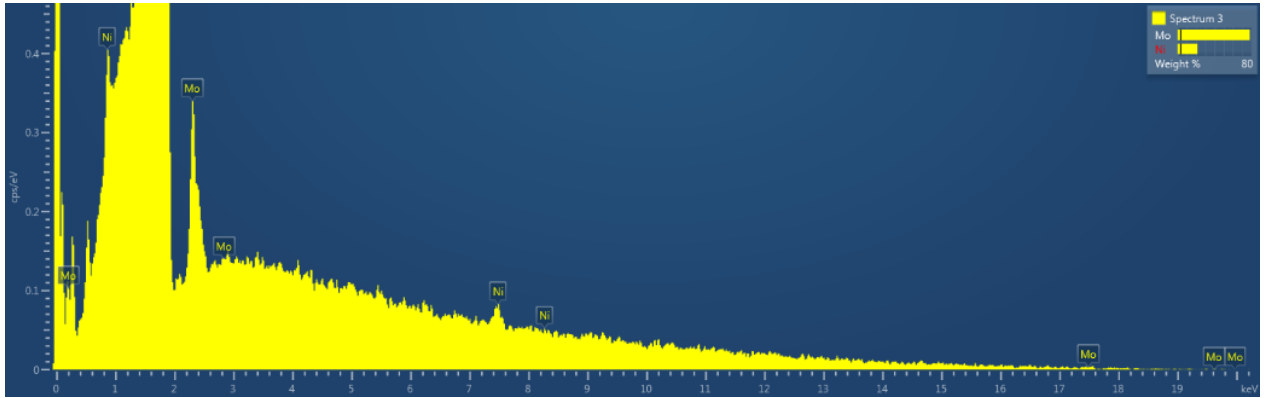
Spectrum 3
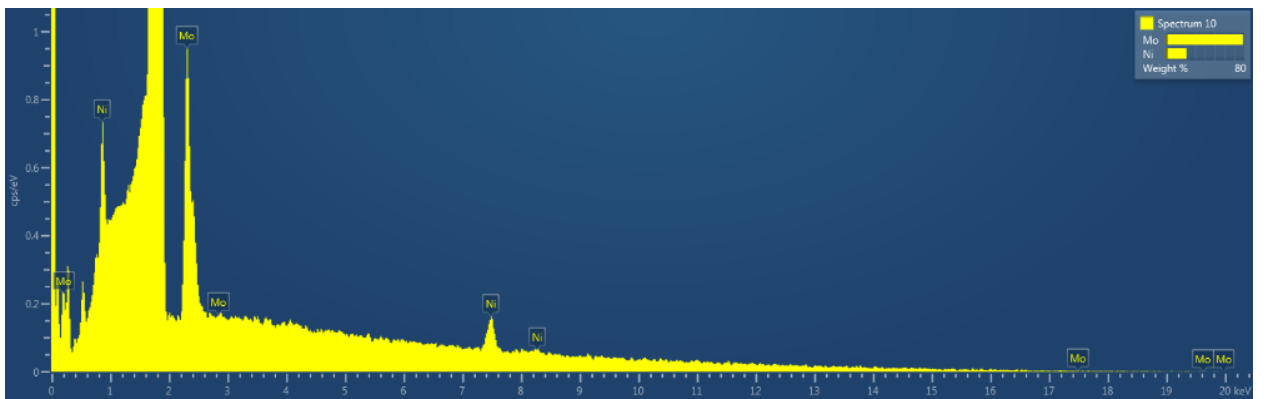
Spectrum 4
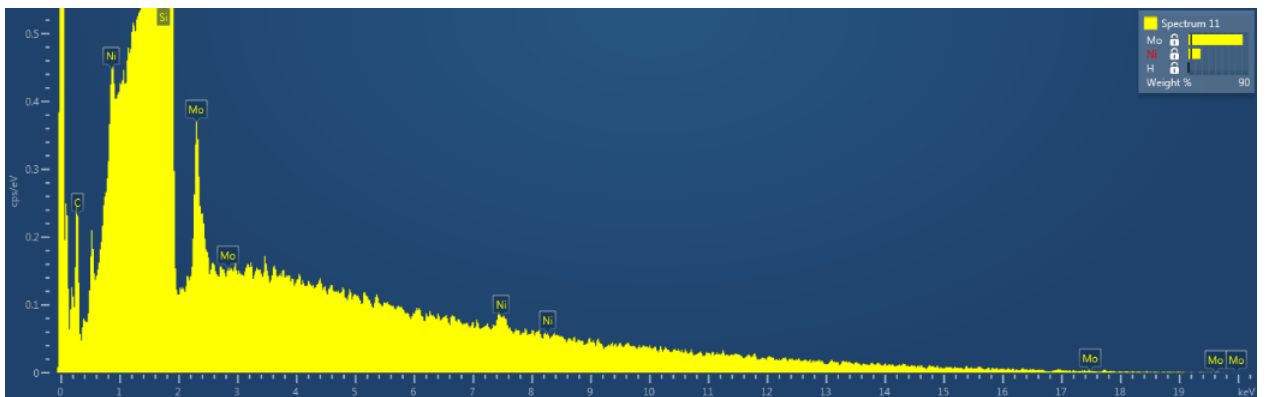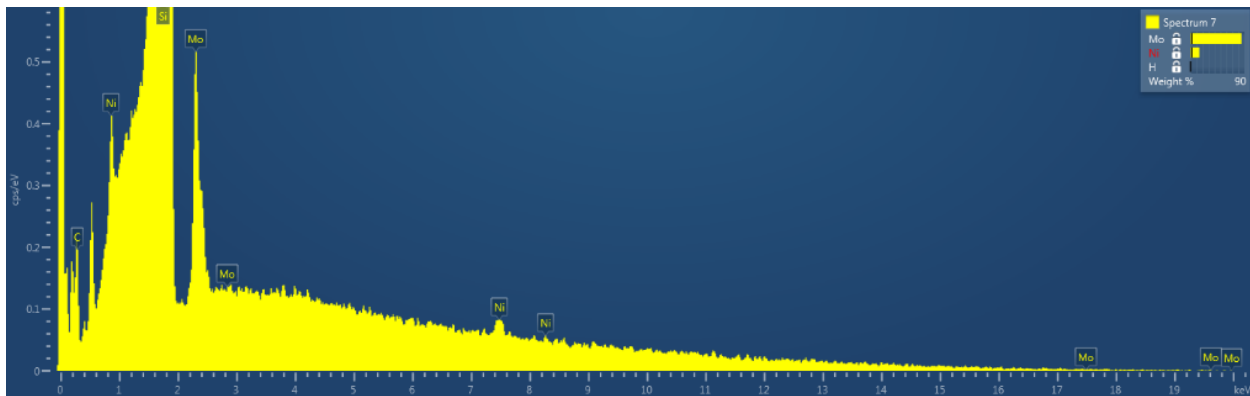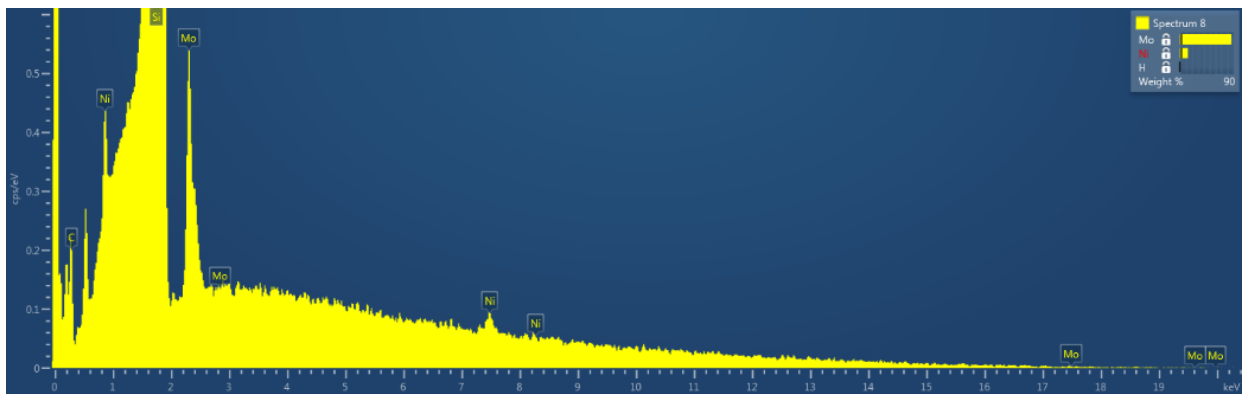

Spectrum 5

Experiment 12

Figure A4. SEM images from experiment 12 with the selected regions for the EDXS characterization marked.
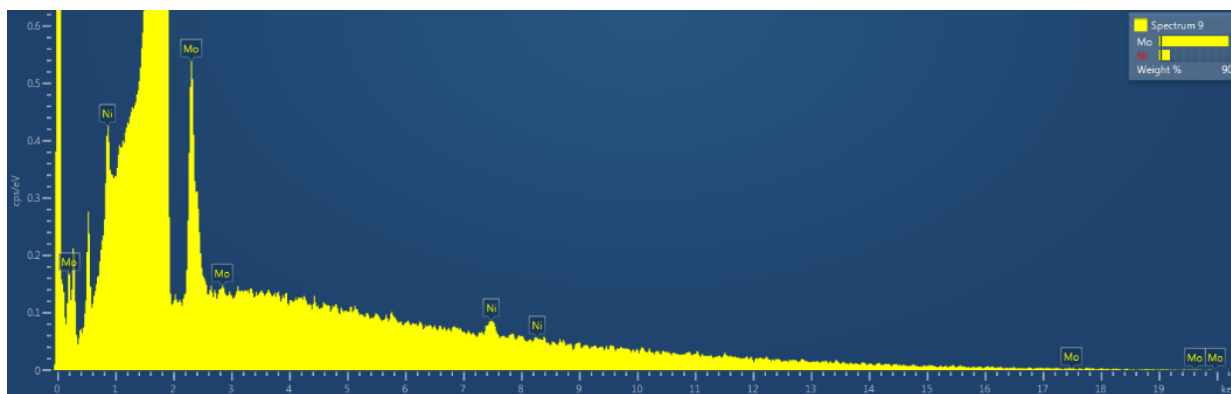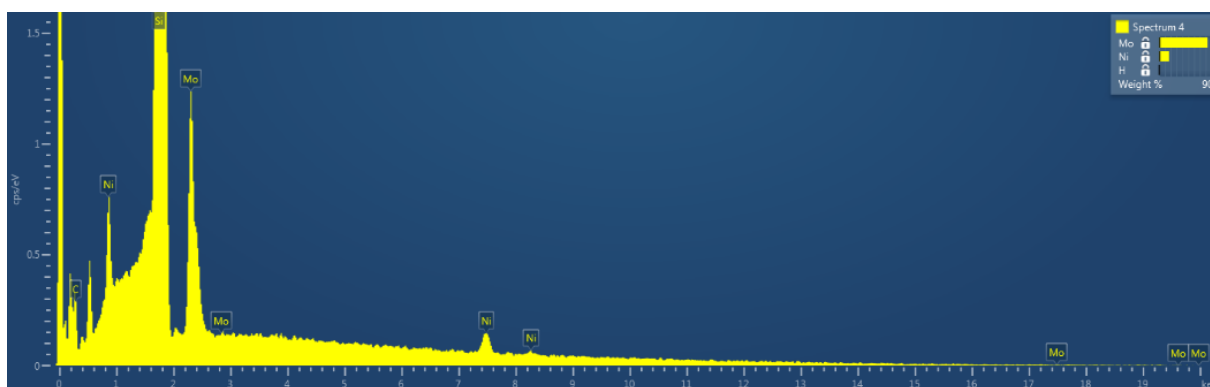
Spectrum 1

Spectrum 2

Spectrum 3

Spectrum 4

Spectrum 5